The Astrophysical Journal, 767:91 (22pp), 2013 April 10 doi:10.1088/0004-637X/767/1/91

A CLUSTER PAIR: A3532 AND A3530

Kiran Lakhchaura[1], K. P. Singh[1], D. J. Saikia[2], and R. W. Hunstead[3]
[1] Department of Astronomy and Astrophysics, Tata Institute of Fundamental Research, 1 Homi Bhabha Road, Mumbai 400 005, India; kiran_astro@tifr.res.in
[2] National Centre for Radio Astrophysics, Tata Institute of Fundamental Research, Pune University Campus, Pune 411 007, India
[3] Sydney Institute for Astronomy, School of Physics, University of Sydney, Sydney, NSW 2006, Australia
Received 2012 July 31; accepted 2013 February 25; published 2013 March 28

ABSTRACT

We present a detailed study of a close pair of clusters of galaxies, A3532 and A3530, and their environments. The *Chandra* X-ray image of A3532 reveals the presence of substructures on scales of ∼20″ in its core. *XMM-Newton* maps of the clusters show excess X-ray emission from an overlapping region between them. Spectrally determined projected temperature and entropy maps do not show any signs of cluster scale mergers either in the overlapping region or in any of the clusters. In A3532, however, some signs of the presence of galaxy scale mergers are visible, e.g., anisotropic temperature variations in the projected thermodynamic maps, a wide-angle-tailed (WAT) radio source in the brighter nucleus of its dumbbell brightest cluster galaxy, and a candidate X-ray cavity coincident with the northwestern extension of the WAT source in the low-frequency radio observations. The northwestern extension in A3532 seems either a part of the WAT or an unrelated diffuse source in A3532 or in the background. There is an indication that the cool core in A3532 has been disrupted by the central activity of the galactic nucleus. A reanalysis of the redshift data reinforces the close proximity of the clusters. The excess emission in the overlapping region appears to be a result of tidal interactions as the two clusters approach each other for the first time. However, we cannot rule out the possibility of the excess being due to the chance superposition of their X-ray halos.

Key words: galaxies: clusters: general – galaxies: clusters: individual (A3532, A3530) – galaxies: clusters: intracluster medium – radio continuum: galaxies – X-rays: galaxies: clusters

Online-only material: color figures

1. INTRODUCTION

Clusters of galaxies are believed to form hierarchically by the merger of smaller groups and clusters. Major cluster mergers, which are believed to be the most energetic events in the universe (Sarazin 2002), involve two clusters of similar masses (Planelles & Quilis 2009). Many clusters are often found to form large concentrations, called superclusters (Shapley 1933), which are the largest (size ∼10–100 Mpc) systems of galaxies known to us (Vogeley et al. 1994). Rich superclusters are also appropriate systems for studying major cluster mergers. The galaxy number density in superclusters is ∼10 times that in the field on length scales of ∼10 h_{100}^{-1} Mpc (Bardelli et al. 2000). This results in high peculiar velocities of the galaxies in superclusters, which increases the probability of cluster–cluster collisions (Bardelli et al. 2001). One such example of a rich supercluster environment is the central region of the Shapley Supercluster (SSC). Raychaudhury et al. (1991), by using X-ray observations from *Einstein Observatory* and *EXOSAT*, and optical data from Automatic Plate Measuring facility at Cambridge, studied 17 clusters from the core region of the SSC. The X-ray data showed an exceptionally high density of rich clusters (∼10–50) and multiple X-ray peaks in most of the clusters belonging to this region. By using the optical data they estimated an exceptionally large mass (between 1.4×10^{16} and 1.6×10^{17} h_{50}^{-1} $M_{\odot}$) for the "core" region (diameter 74 h_{50}^{-1} Mpc) of the SSC. The optical data also revealed a large deviation from the Hubble flow within the SSC which suggested that it might be a nearly bound system. By using the X-ray observations from the *ROSAT* All Sky Survey, de Filippis et al. (2005) discovered 14 new cluster candidates, and also observed that the overdensity of clusters in the SSC outskirts is mainly due to an excess of low X-ray luminosity clusters. This led to a suggestion that the whole region is still accreting small clusters with low luminosities from the outskirts (de Filippis et al. 2005).

The SSC hosts two major cluster complexes dominated by A3558 and A3528. This concentration of clusters is a rich system for observing cluster mergers at various evolutionary stages (Bardelli et al. 2001). The A3558 complex comprises three rich clusters of galaxies, viz., A3556, A3558, and A3562, and several other poor clusters and groups, while the A3528 complex is formed by the galaxy clusters A3528, A3532, and A3530. The properties of the A3558 complex have been extensively studied using multiwavelength studies (optical: Bardelli et al. 1994, 1998a, 1998b; radio: Venturi et al. 1997, 1998, 2000; X-ray: Bardelli et al. 1996; Ettori et al. 2000). The less well-studied A3528 cluster complex has a mean redshift of $\overline{z} = 0.0535$ and is elongated in the north–south direction. Using *ROSAT* Position Sensitive Proportional Counter (PSPC) observations, Schindler (1996) found that A3528 is a double cluster comprising A3528N and A3528S. Using a redshift survey of galaxies, Bardelli et al. (2001) detected substructures in the A3528 complex by using the non-parametric and scale-independent DEDICA method (Pisani 1993, 1996) in both bi-dimensional and three-dimensional (3D) samples. From the bi-dimensional sample the cluster A3528 was found to contain a total of ten groups, two of which appear to be associated with A3528N and A3528S. From the 3D sample, the A3532–A3530 system was found to contain five groups, out of which two seem to be associated with A3530 and A3532, while two others are found at the intersection of the Abell radii of the two clusters, with a mean velocity in agreement with the main components. The cluster complex has been studied in the radio by Venturi et al. (2001) using 13 cm and 22 cm observations carried out with the Australia Telescope Compact Array (ATCA). Mauduit & Mamon (2007) studied the radio continuum emission from galaxies in the SSC core

region and found that the galaxies in the A3528 complex are marginally more radio luminous than elsewhere, contrary to what is observed in the neighboring A3558 cluster complex, where the galaxies have lower radio luminosity and radio loudness compared to the field galaxies. They have attributed the decrease in the radio loudness in the A3558 cluster complex to starvation of the active galactic nucleus (AGN) in them, and reduced star formation activity due to the enhanced ram pressure stripping in merging clusters. The lack of decrease in the radio loudness for the A3528 cluster complex is, therefore, probably because in this region the clusters are approaching for the first time (Mauduit & Mamon 2007). In this paper, we present a detailed study of the environments, interactions, and internal dynamics of the two less well-studied clusters of galaxies, viz., A3530 and A3532, from the A3528 cluster complex, using mainly radio and X-ray observations.

The paper is organized as follows. Detailed information about the two clusters and a summary of their previous X-ray, radio, and optical observations are given in Section 2. Details of the X-ray and radio observations used here, along with the data reduction, are presented in Section 3. The X-ray, optical, and radio morphologies of the clusters are described in Section 4.1. Results from the global spectral analyses and the X-ray luminosity estimates are provided in Sections 4.2 and 4.3, respectively. Results from the azimuthally averaged (projected and deprojected) spectral analyses and the two-dimensional (2D) projected thermodynamic maps of the clusters are described in Sections 4.4 and 4.5, respectively. The estimates of the cooling time, gas mass, and virial mass for the two clusters are given in Sections 4.6, 4.7, and 4.8, respectively. A discussion based on the results is in Section 5. A lambda cold dark matter cosmology with $H_0 = 70$ km s^{-1} Mpc^{-1} and $\Omega_M = 0.3$ ($\Omega_\Lambda = 0.7$) has been assumed throughout.

2. THE A3530–A3532 SYSTEM

Both A3532 and A3530 are regular clusters of richness class 0, with 36 and 34 member galaxies, respectively (Abell et al. 1989). The positional coordinates (R.A.(J2000), decl.(J2000)) of A3532 are $12^h57^m19\overset{s}{.}2$, $-30^d22'13''$ (Mahdavi & Geller 2001), and those of A3530 are $12^h55^m36^s$, $-30^d21\overset{'}{.}2$ (Abell et al. 1989). A3532 and A3530 are located at mean redshifts of $\bar{z} = 0.0554 \pm 0.0004$ (Cristiani et al. 1987) and $\bar{z} = 0.0543 \pm 0.0009$ (Vettolani et al. 1990), respectively. The total mass (M_{500}) (sum of baryonic and non-baryonic mass within R_{500}, i.e., radius within which the mean density of the cluster equals 500 times the critical density) estimates of A3532 and A3530, reported by Ettori et al. (1997), based on an image deprojection analysis done using *ROSAT* PSPC images, are $6.38 \times 10^{14}\ h_{50}^{-1}\ M_\odot$ and $4.69 \times 10^{14}\ h_{50}^{-1}\ M_\odot$, respectively. Bardelli et al. (2001) reported that the projected distance between the centers of A3530 and A3532 is smaller than the sum of their virial radii, thus indicating a tidal interaction between the two clusters. It should, however, be noted that, if the redshift difference between the two clusters ($\triangle z \sim 0.0010 \pm 0.0009$) is entirely due to Hubble flow, then the difference in their line-of-sight distances is $4.2 \pm 3.7\ h_{70}^{-1}$ Mpc, which can be larger than the sum of their virial radii ($\sim 3\ h_{70}^{-1}$ Mpc). This means that it is possible that the two clusters do not actually overlap. However, a tidal interaction between them is still possible and they may form a bound system. Various estimates of the temperatures and X-ray luminosities of the two clusters can be found in the literature (Raychaudhury et al. 1991; Ettori et al. 1997; McCarthy et al. 2002; Reiprich & Böhringer 2002). However, the results obtained by Ikebe et al. (2002) used *ASCA* with the energy band closest to *Chandra* and *XMM-Newton*. By fitting 2-T thermal plasma models to the *ASCA* spectra of A3532 and A3530, Ikebe et al. obtained hot component temperatures of 4.4 ± 0.2 and 4.1 ± 0.3 keV, and 0.1–2.4 keV X-ray luminosities of $(5.9 \pm 0.2) \times 10^{43}\ h_{100}^{-2}$ ($= (12.0 \pm 0.4) \times 10^{43}\ h_{70}^{-2}$) and $(3.3 \pm 0.2) \times 10^{43}\ h_{100}^{-2}$ ($= (6.6 \pm 0.3) \times 10^{43}\ h_{70}^{-2}$) erg cm^{-2} s^{-1}, respectively. Note that Ikebe et al. have provided the temperature values of the hot components only, as these are the temperatures of the main extended emission components of the clusters and, therefore, are good measures of the virial temperatures of the clusters (Ikebe et al. 2002). A comparison of the values obtained by Ikebe et al. with those obtained from our analysis has been made in Table 3.

By using *ASCA* and *ROSAT* observations, Chen et al. (2007) identified both A3532 and A3530 as non-cool core (NCC) clusters with cooling times of $(2.4^{+0.5}_{-0.4}) \times 10^{10}$ and $(5.3 \pm 0.6) \times 10^{10}\ h_{50}^{-1/2}$ yr, respectively. The virial radii R_{200} of A3532 and A3530, computed by Vulcani et al. (2011), using their respective velocity dispersions of 621 ± 53 km s^{-1} and 563 ± 52 km s^{-1} (Cava et al. 2009), are $1.50\ h_{50}^{-1}$ Mpc and $1.36\ h_{50}^{-1}$ Mpc, respectively.

A3530 is seen to host a pair of elliptical brightest cluster galaxies (BCGs) at its center (Venturi et al. 2001), whereas A3532 is found to be dominated by a dumbbell system of BCGs at the center (Wirth et al. 1982; Parma et al. 1991; Machacek et al. 2007; Gregorini et al. 1994). Pimbblet (2008) studied a complete sample of dumbbell galaxies in the southern rich clusters listed in Gregorini et al. (1994), and found that while most of the dumbbell BCGs (including that in A3532) have at least one dumbbell component with a significant peculiar velocity, the absence or presence of subclustering in the dumbbell BCG clusters is due to the different states of post-merger activity.

Clusters of galaxies are found to host a wide variety of radio source morphologies, such as the characteristic wide-angle-tailed (WAT) structure (Owen & Rudnick 1976; Roettiger et al. 1996; Douglass et al. 2008; Mao et al. 2009). Especially, the dumbbell galaxy systems, as seen in A3532, are very often seen to host radio sources in one or both of their members. A WAT radio source is indeed associated with the brighter nucleus of the dumbbell BCG in A3532 in the ATCA 13 cm and 22 cm images (Venturi et al. 2001). Close proximity of the galaxies ($\sim$10–30 h_{70}^{-1} kpc) in the dumbbell systems can dynamically affect the radio jets through gravitational interaction with the confining gas cloud (Wirth et al. 1982). Here, it should be noted that the separation between the dumbbell galaxies in A3532 is only $\sim 25\ h_{70}^{-1}$ kpc in projection. The radio sources associated with the dumbbells are often found to be different from single galaxy radio sources because of their more distorted (irregular) structures, and flatter radio luminosity functions, indicating a triggering of the radio source in the main galaxy by its close companion (Parma et al. 1991; Gregorini et al. 1994), or alternatively causing an increase in the luminosity of the existing radio source (Parma et al. 1991). The total radio flux densities estimated for the WAT source in A3532 at 13 cm and 22 cm, as reported by Venturi et al. (2001), are 651.7 mJy and 1056.6 mJy (with errors $\sim$10%–15%), respectively. Combining these with the 6 cm flux density of the source as given in Gregorini et al. (1994), Venturi et al. also computed the spectral index $\alpha \sim 0.85$, for the 6–22 cm wavelength range.

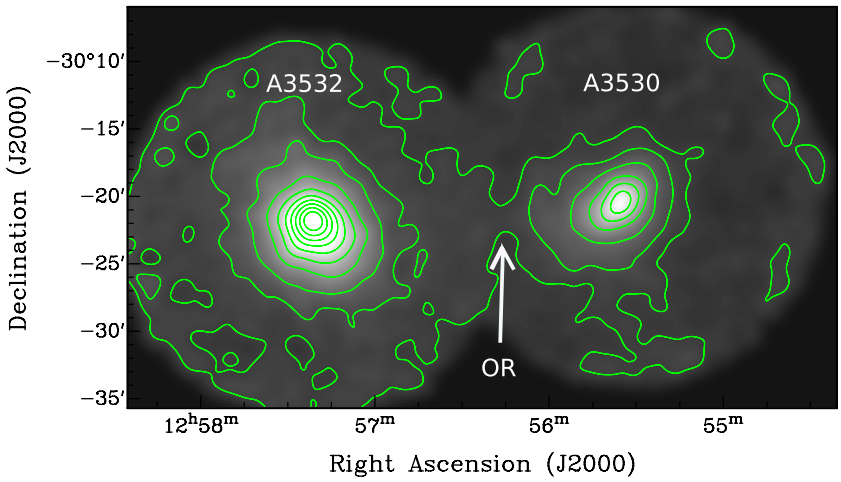

Figure 1. Combined and contoured image of A3532 and A3530 clusters from the *XMM-Newton* MOS detectors, smoothed with a Gaussian kernel of width 35″, as described in Section 3.1.1.2. Contour levels are (1.25, 1.69, 2.50, 3.75, 5.00, 6.25, 7.50, 8.75, 10.00, 11.25) $\times 10^{-8}$ counts s^{-1} $arcsec^{-2}$. Positions of the clusters A3532 and A3530, and their overlapping region (OR) are shown. The surface brightness peaks of the two clusters are separated by approximately 1.7 Mpc. The outermost contour is about 3σ level above the neighboring local background.

(A color version of this figure is available in the online journal.)

Table 1
X-Ray Observations for A3530 and A3532

Cluster	Satellite	Detector	α (J2000)	δ (J2000)	Observation ID	Date of Observation	Exposure Time
A3532	*XMM-Newton*	MOS1, MOS2, PN	12 57 16.85	−30 22 11.1	0030140301	2002 Jul 3	16.9 ks
A3532	*Chandra*	ACIS-I	12 57 21.50	−30 22 10.	10745	2008 Nov 30	9.8 ks
A3530	*XMM-Newton*	MOS1, MOS2, PN	12 55 35.87	−30 19 51.4	0201780101	2004 Jan 15	21.9 ks

3. OBSERVATIONS AND DATA REDUCTION

The cluster A3532 has been observed with both *XMM-Newton* and *Chandra*, whereas A3530 has only been observed using *XMM-Newton*. A journal of the X-ray observations is given in Table 1. Throughout Sections 3 and 4, we have adopted an average redshift of 0.0554 (Cristiani et al. 1987) for A3532 and 0.0543 (Vettolani et al. 1990) for A3530.

3.1. X-Ray Data

3.1.1. XMM-Newton

A3532 and A3530 were observed with *XMM-Newton* on 2002 July 3 and 2004 January 15, respectively (see Table 1). For both the observations, the three EPIC cameras MOS1, MOS2 (Turner et al. 2001), and PN (Strüder et al. 2001) were operated in the full frame mode with the medium filter. The data were obtained from the HEASARC archives.

All data analyses have been done following the standard procedures from the Science Analysis System (SAS) software version 11.0.0. The good time intervals (GTIs), obtained after the initial filtering of the MOS1, MOS2, and PN observations of A3530, are 11.4 ks, 11.5 ks, and 10.2 ks, respectively, while for A3532 the GTIs are 7.4 ks and 7.9 ks for the observations done using MOS1 and MOS2, respectively. The PN observation of the cluster A3532 was strongly affected by soft proton (SP) flares. Only 4.7 ks (of the total exposure time of 16.9 ks) exposure was left after the light curve cleaning, which was still likely to be contaminated with residual SPs. Hence, the PN observations of A3532 were found unusable for the study.

3.1.1.1. Background Treatment. The residual SP contamination, left after the routine temporal filtering was modeled as described in Snowden et al. (2008). The quiescent particle-induced background and the cosmic background component were removed by using the blank-sky observations described in Carter & Read (2007). The blank-sky event files were filtered as described in Lakhchaura et al. (2011). Local background subtraction could not be done for either observation, since the sources fill almost the entire field of view of the detectors and emission-free regions were difficult to find.

3.1.1.2. Point-source Removal and Mosaicking. Point sources were detected and removed using the SAS task *cheese*. Each of the detected sources was then checked in the MOS detector images of both the clusters and spurious sources (detections that did not look like real sources in the images) were removed. Finally, a total of 26 sources for the cluster A3532 and 12 sources for the cluster A3530 were confirmed. Images and exposure maps were created from the filtered and point-source-removed event files from MOS observations of both the clusters in the energy band 0.3–9 keV. From these, the mosaicked and exposure-corrected image with a pixel bin size of 5″ was created using the SAS task *emosaic*. The final contour map of the diffuse X-ray emission after smoothing with a Gaussian kernel of width 35″ is shown in Figure 1. Note that the galaxy groups found by Bardelli et al. (2001; see Section 1), at the intersections of the Abell radii of A3532 and A3530, have not been covered by either of the two *XMM-Newton* pointings. An overlay of the X-ray contours (black) superimposed on an optical image of the two clusters from the SuperCOSMOS survey in the B_J band is shown in Figure 2.

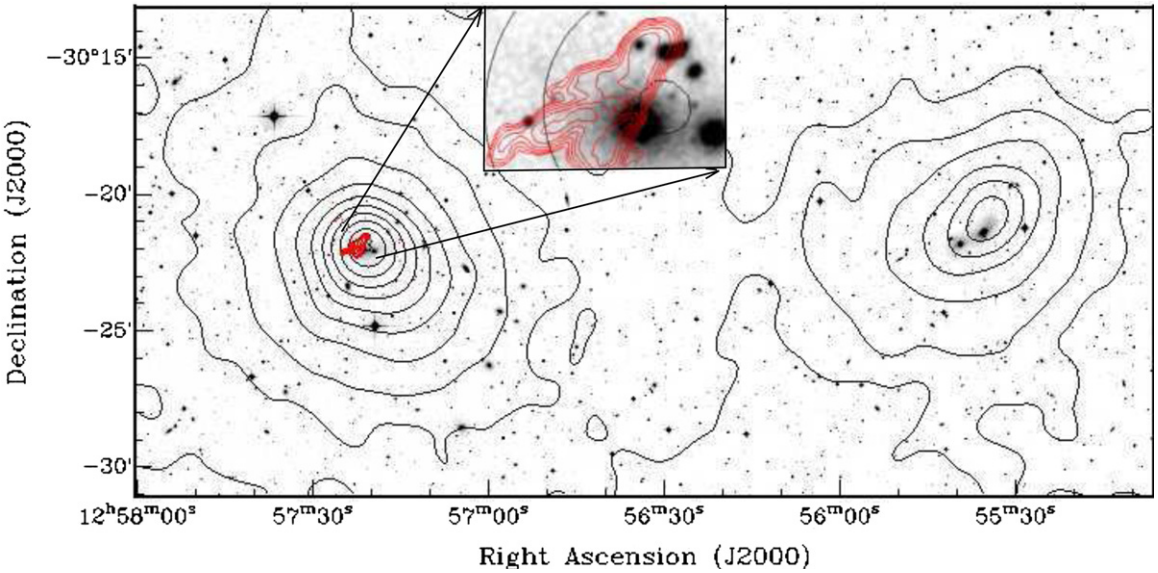

Figure 2. Combined image of the clusters A3532 and A3530 from the SuperCOSMOS survey in the B_J band, overlaid with the X-ray contours (black) from Figure 1 and also with the VLA 20 cm contours (red, contour levels: −0.3, 0.3, 0.6, 1.2, 2.4, 4.8, 9.6, 19.2, and 38.4 mJy beam^{-1}).

(A color version of this figure is available in the online journal.)

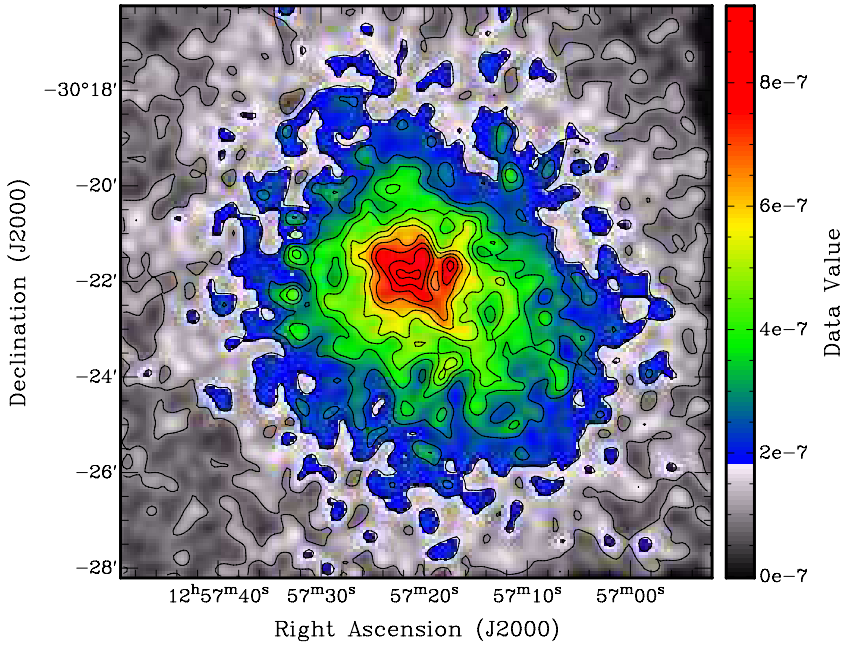

Figure 3. Exposure-corrected *Chandra* ACIS image of the A3532 cluster in the 0.3–7.0 keV band (after point-source removal and smoothing with a Gaussian kernel of width 8″). The overlaid X-ray emission contours (black) are linearly distributed between 1×10^{-7} and 9×10^{-7} counts cm^{-2} s^{-1} pixel^{-1}.

(A color version of this figure is available in the online journal.)

3.1.2. *Chandra*

A3532 was observed with *Chandra* on 2009 December 2 with ACIS-I detector for 9.8 ks (Table 1). For the analysis of *Chandra* data, we have used CIAO version 4.3 and CALDB version 4.4.0. The data were reprocessed using the CIAO script *chandra_repro*. For all the GTIs, no significant flaring was seen in the light curves. Point sources were detected using the CIAO task *celldetect*, which were then checked by comparing them with those detected with *XMM-Newton* and with the ones seen in the optical image (Figure 2). The confirmed point sources were then removed from both the image and the event files and the holes created in the image were filled with values equal to the average counts in their immediately surrounding pixels, using the CIAO task *dmfilth*. The image was then exposure corrected and smoothed using a Gaussian kernel of width 8″. The resultant image is shown in Figure 3.

3.2. *Radio Data*

We have analyzed archival data from pointed observations of A3532 with the ATCA, the Giant Metrewave Radio Telescope (GMRT), and the Very Large Array (VLA). In addition to the pointed observations, we have used survey data from the TIFR (Tata Institute of Fundamental Research) GMRT Sky Survey (TGSS), the NRAO (National Radio Astronomy Observatory) VLA Sky Survey (NVSS), the Sydney University Molonglo Sky

Table 2
Radio Observations for A3532 WAT

Observation	Wavelength (m)	Beam Size	Position Angle	Array Configuration	Date of Observation	rms (mJy beam^{-1})	Flux Density (Jy)	Reference
VLA	0.06	$13\farcs37 \times 9\farcs66$	−54.49	VLA-DnC	1991 Feb 5	0.035	0.36 ± 0.02	P
ATCA	0.13	$6\farcs28 \times 4\farcs08$	−0.26	6C	1994 Mar 15	0.3	0.69 ± 0.03	P
VLA	0.20	$4\farcs87 \times 2\farcs91$	−52.73	VLA-BnA	1990 Jul 9	0.12	1.05 ± 0.05	P
VLA (NVSS)	0.21	$45'' \times 45''$	0	...	...	0.48	1.16 ± 0.04	1
ATCA	0.22	$10\farcs72 \times 6\farcs45$	0.02	6C	1994 Mar 15	0.4	1.06 ± 0.05	P
MOST (SUMSS)	0.36	$85'' \times 45''$	0.0	...	...	1.8	1.78 ± 0.05	2
GMRT	0.50	$7\farcs45 \times 4\farcs62$	28.90		2004 Apr 4	0.13	1.9 ± 0.3	P
Molonglo Cross (MRC)	0.74	$2\farcm87 \times 2\farcm62$	0.0	...	...	50	3.03 ± 0.08	3
GMRT (TGSS)	2.0	$24'' \times 15''$	30	...	...	23	8.7 ± 2.2	4
VLA (VLSS)	4.0	$58\farcs8 \times 36\farcs2$	−47.9	...	...	102	11.7 ± 1.2	5

Notes. (a) Errors of ∼5% have been assumed for both the ATCA observations, the VLA 1.49 and 4.86 GHz observations. For the GMRT TGSS and 608 MHz observations errors of ∼25% and ∼15% have been assumed, respectively. (b) For the ATCA observations, the pointing center (R.A. (J2000), decl. (J2000)) was $12^h57^m13\fs0$, $-30°23'44''$ (J2000), the bandwidth was 128 MHz, and the total integration time was approximately 2 hr. For the GMRT observations, the pointing center for the observation was $12^h56^m30^s$, $-30°30'$ (J2000), the bandwidth was 16 MHz, and the total integration time was about 2 hr 12 minutes. For the VLA *L*-band and *C*-band observations, the pointing centers were $12^h57^m20\fs85$, $-30°21'51\farcs64$ and $12^h57^m21\fs99$, $-30°21'47\farcs42$, and the total integration times were ∼25 minutes and ∼15 minutes, respectively. The bandwidth for both observations was 50 MHz.
References. (P) Present paper; (1) Condon et al. 1998; (2) Mauch et al. 2003; (3) Large et al. 1981; (4) TGSS Data Products; (5) Cohen et al. 2007.

Survey (SUMSS), the Molonglo cross telescope, and the VLA Low-frequency Sky Survey (VLSS). All details of the radio observations are given in Table 2.

The ATCA observations were made simultaneously at 1380 and 2378 MHz in multiple-cut mode. The primary flux density calibrator was B1934−638 and the phase calibrator was B1308−220. Data reduction was carried out in MIRIAD (Sault et al. 1995) using standard techniques. The GMRT observation at 614 MHz was made with 3C286 as primary flux density calibrator and J1311−222 as phase calibrator. The VLA observations were made with two intermediate frequencies, bandwidths of 50 MHz, and center frequencies of 1490 MHz and 4860 MHz. The primary flux density calibrator for both VLA observations was 3C286, and the phase calibrators were B1245−197 and B1255−316. The GMRT and VLA data were both processed using the NRAO Astronomical Image Processing System software and standard procedures. Figures 4(a)–(g) show the radio images produced from the VLA 20 cm, ATCA 13 cm, GMRT 50 cm, VLA 6 cm, TGSS 2 m, VLSS 4 m, and SUMSS 36 cm observations, respectively.

4. ANALYSIS AND RESULTS

4.1. X-Ray, Optical, and Radio Maps

The smoothed and point-source-removed X-ray image of the two clusters A3530 and A3532 from the *XMM-Newton* MOS (MOS1 + MOS2) detectors (Section 3.1.1.2, Figure 1) shows that the X-ray emission from A3532 fills the entire field of view and is slightly elliptical with the major axis oriented along the NE–SW direction (∼45° to the north). X-ray emission from A3530 is much less extended but much more elongated along the NW–SE direction (∼−52° to the north). The X-ray contours in the inner parts of A3532 seem to be compressed toward the NE and stretched out toward the SW, and those of A3530 seem to be stretched out toward the SE. The projected separation between the X-ray peaks of the two clusters is ∼26.′5, which, at their average redshift, corresponds to a linear projected separation of ∼1.7 Mpc. The X-ray contours of the two clusters overlap in a region common to both clusters (marked in Figure 1), where they may be tidally interacting with each other. Like *XMM-Newton*, the *Chandra* image of A3532 also shows an elongation of the X-ray emission in the NE–SW direction with the X-ray contours stretching out more toward the SW than in the NE direction (Figure 3). The inner parts of the *Chandra* image show very disturbed morphology with multiple peaks and subpeaks. This is discussed in detail in Section 4.9.

The overlay of the X-ray contours on the optical image of the two clusters from the SuperCOSMOS survey in the B_J band is shown in Figure 2. It can be seen that the X-ray emission peaks of both clusters coincide with the positions of their respective BCGs. The 20 cm radio contours (red) in Figure 2 show a "C"-shaped WAT source at the center of A3532, coincident with the position of the brighter nucleus of its dumbbell BCG. In Figure 4, the WAT source is seen at all the radio wavelengths with sufficient angular resolution. The projected radio emission of the WAT galaxy is aligned in the NW–SE direction, i.e., approximately orthogonal to the major axis of the X-ray emission. The structure of the WAT is complicated somewhat by our viewing angle. It comprises two hot spots (locations of enhanced radio emission caused by the sudden slowing of the relativistic electrons as they emerge from the host galaxy into the intracluster medium, ICM) "H1" and "H2", and two closely aligned tails "T1" and "T2" (Figure 4(a)), trailing back from the hot spots. The GMRT 50 cm, TGSS 2 m, and SUMSS 36 cm images (Figures 4(c), (e), and (g), respectively) show an extension of the radio emission in the northwest direction. The VLSS observation also shows some emission in this part of the WAT but it is not well resolved.

In Figures 4(a)–(c), the tails of the WAT source appear to be very closely aligned and seem to eventually merge with each other. This makes the apparent morphology of the source intermediate to that of a WAT and a narrow-angle-tailed (NAT) source. However, the NAT sources are usually associated with galaxies found at the cluster peripheries with their tails highly bent as a result of very high velocity ($\gtrsim$ a few thousand km s^{-1}) motions of the host galaxies through the relatively stationary ICM (Jones & Owen 1979; Klamer et al. 2004; Mao et al. 2009). On the other hand, the dominant cluster galaxies with which the WAT sources (like the one in A3532) are associated do not have peculiar velocities more than a few hundred km s^{-1} and, therefore, the ram pressure due to the galaxy's motion is not very high (Burns 1981; Eilek et al. 1984; O'Donoghue et al.

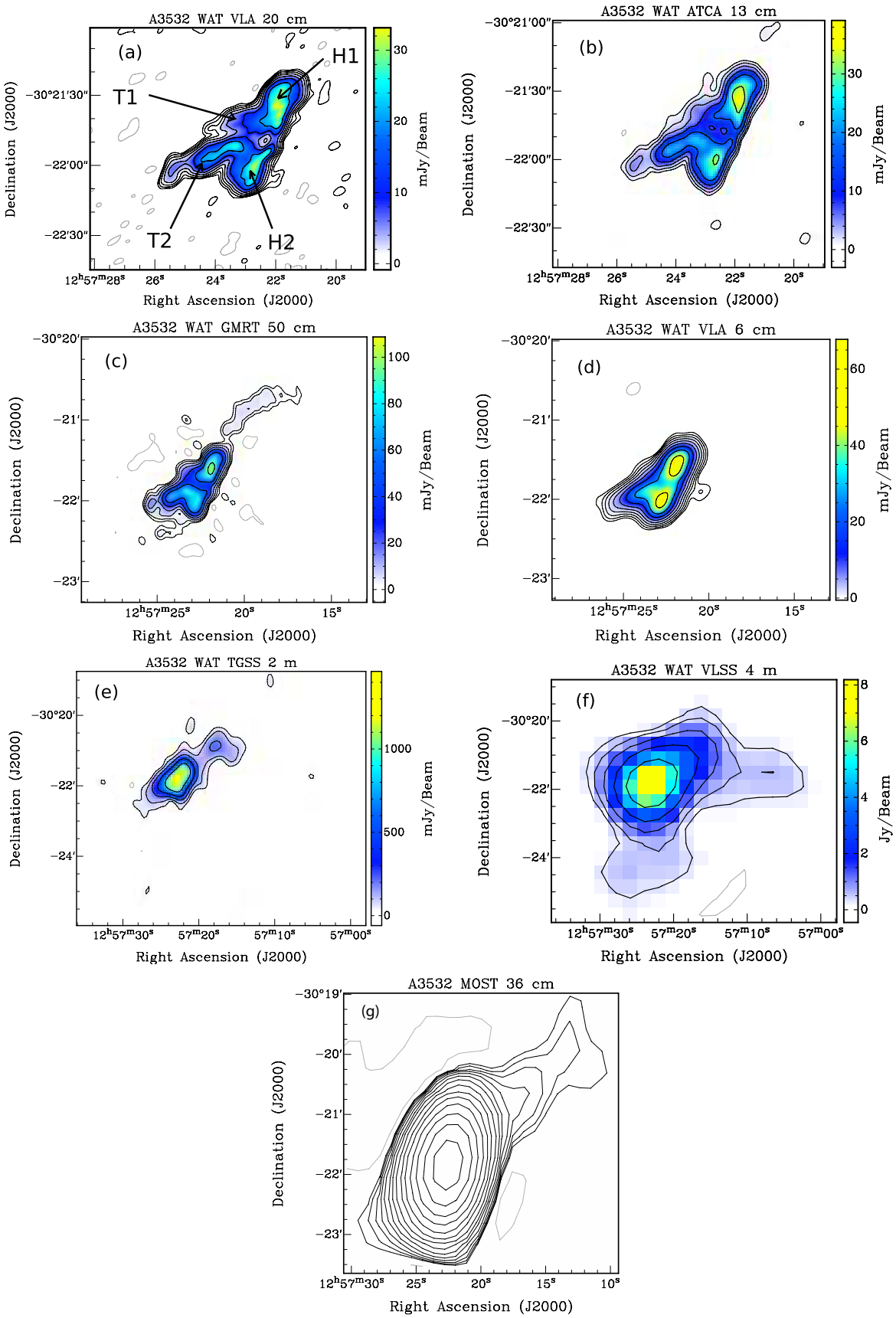

Figure 4. Contoured radio images of the WAT source in A3532 from (a) VLA 20 cm, (b) ATCA 13 cm, (c) GMRT 50 cm, (d) VLA 6 cm, (e) TGSS 2 m, and (f) VLSS 4 m observations, with the contour levels starting at 0.3, 1, 1.5, 0.2, 50, and 300 mJy beam^{-1}, respectively, and increasing by factors of two. (g) The contoured image of the WAT source from SUMSS 36 cm observation, with contour levels starting at 12 mJy beam^{-1} and increasing by factors of $\sqrt{2}$. The images have been arranged in increasing order of beam sizes. The hot spots "H1" and "H2", and tails "T1" and "T2" of the WAT source, are marked in (a).

(A color version of this figure is available in the online journal.)

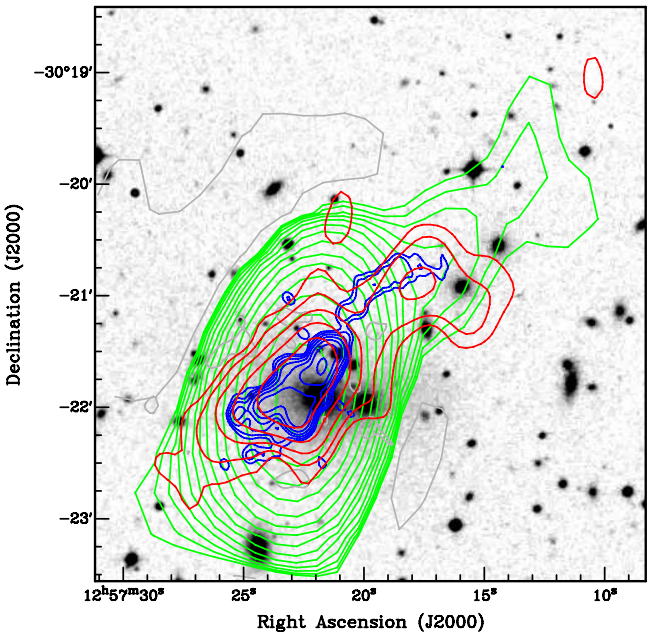

Figure 5. GMRT 2 m (TGSS; red) and 50 cm (blue), and SUMSS 36 cm (green) contours overlaid on the optical image of the central part of A3532 from the SuperCOSMOS survey. The northwestern extensions of the WAT source seen in the three sets of radio contours seem to coincide.

(A color version of this figure is available in the online journal.)

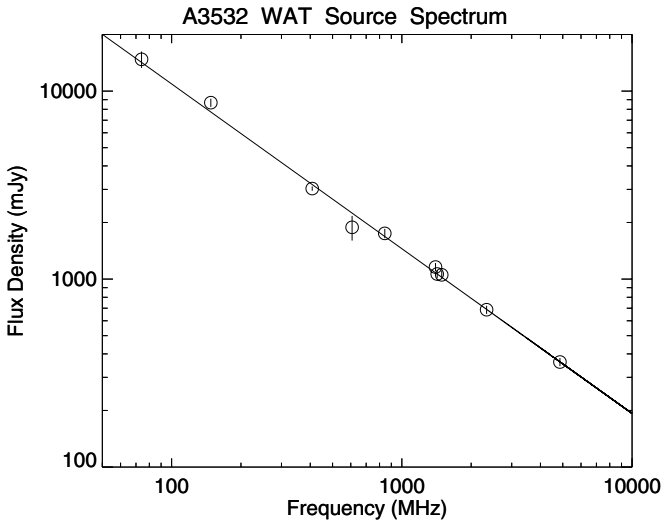

Figure 6. Radio spectrum of the complete WAT source in A3532 on a log–log scale, fitted with a power-law model. The flux densities used and the details of the observations are given in Table 2.

1990). It is also quite unlikely that the ram pressure from the ICM (resulting from the motions induced by the galaxy scale mergers), which is generally responsible for the bent tails of the WAT sources (Eilek et al. 1984; Burns et al. 1994; Roettiger et al. 1996), could lead to the observed alignment of the WAT tails in A3532. Considering these facts, a likely interpretation is that the plane of the WAT is aligned at a small angle to our line of sight and the observed close alignment of the tails is due to the projection effects.

The northwestern extension of the radio emission is only seen at the lowest frequencies. Figure 5 shows the GMRT 50 cm, TGSS 2 m, and SUMSS 36 cm contours overlaid on the optical image of A3532. The northwestern extensions seen in the three sets of contours seem to coincide, strengthening the reality of the feature. However, the exact shapes and extents of these extensions do not match, mostly due to the different beam sizes. It should also be noted that in the TGSS survey observation, each source is observed for a very short duration of time (∼3.5 minutes) and therefore the final image may have certain artifacts. The extension does not seem to have an optical counterpart, therefore it may either be a part of the WAT radio emission or a diffuse source unrelated to the WAT, e.g., a radio relic in the cluster or a background source. Using the flux density estimates obtained from the GMRT 50 cm, TGSS, and SUMSS observations, the extension is found to have a steep spectrum with a power-law spectral index, $\alpha \sim -2$. Deeper and high-resolution radio observations at lower frequencies will be required to make a detailed study of the morphology and spectral properties of the extension.

The estimated rms and flux densities of the full WAT source obtained from observations at various frequencies are given in Table 2. The spectrum of the WAT source (as shown in Figure 6) is consistent with a single power law with a spectral index α of -0.88 ± 0.02 ($S_\nu \propto \nu^\alpha$). The flux density of the WAT source obtained from the 50 cm GMRT observation seems to be a bit low, even after correcting for the primary beam pattern using the standard GMRT values. In this archival data set, the source was observed about 15′ away from the phase center, and this along with the low declination of the source accounts for the large flux density error of ∼15%. Also, the 20 cm flux densities obtained from the VLA and ATCA seem to be slightly low, compared with that from the NVSS, possibly as a result of missing flux in high-resolution images.

4.2. Global X-Ray Spectra

We extracted *XMM-Newton* spectra averaged over the cluster sizes for each of the clusters A3532 and A3530, and for the overlapping region (OR) between them. For A3532 and A3530, spectra were extracted from circular regions (radii ∼9.′6 and 7.′9, respectively) centered on their respective X-ray emission peaks. For the OR the spectra were extracted from a small elliptical region, common to both A3530 and A3532. For A3532, spectra from *Chandra* were also extracted. As *Chandra* did not cover the full circular region that was used to extract the *XMM-Newton* spectra of A3532, a polygon-shaped approximation to the circular region was made to extract the *Chandra* spectrum. For this spectrum, an emission-free region near the cluster was used for extracting the background spectrum. The extraction of the background spectrum for the *XMM-Newton* observations is described in Section 3.1.1.1.

The X-ray spectral fitting package *XSPEC* (version 12.5.1) was used for all the spectral analyses. All spectra were fitted in the energy band 0.5–8.0 keV. The neutral hydrogen column densities along the line of sight to A3532 and A3530 were fixed to be 6.47×10^{20} cm^{-2} and 6.24×10^{20} cm^{-2}, respectively, based on Leiden/Argentine/Bonn Galactic H I survey (Kalberla et al. 2005) and the redshifts were frozen to their average values for the respective clusters. The *wabs* photoelectric absorption model (Morrison & McCammon 1983) and *apec* plasma emission model (Smith et al. 2001) have been used for fitting all the spectra. The relative elemental abundances given in Anders & Ebihara (1982) were used for *wabs*. For *XMM-Newton* analyses, the MOS1, MOS2, and PN (only MOS1 and MOS2 for A3532) spectra were fitted simultaneously using three separate *wabs***apec* models. For the spectra belonging to the same region, the values of abundance, temperature, and *apec* normalizations for the models were linked together but were kept

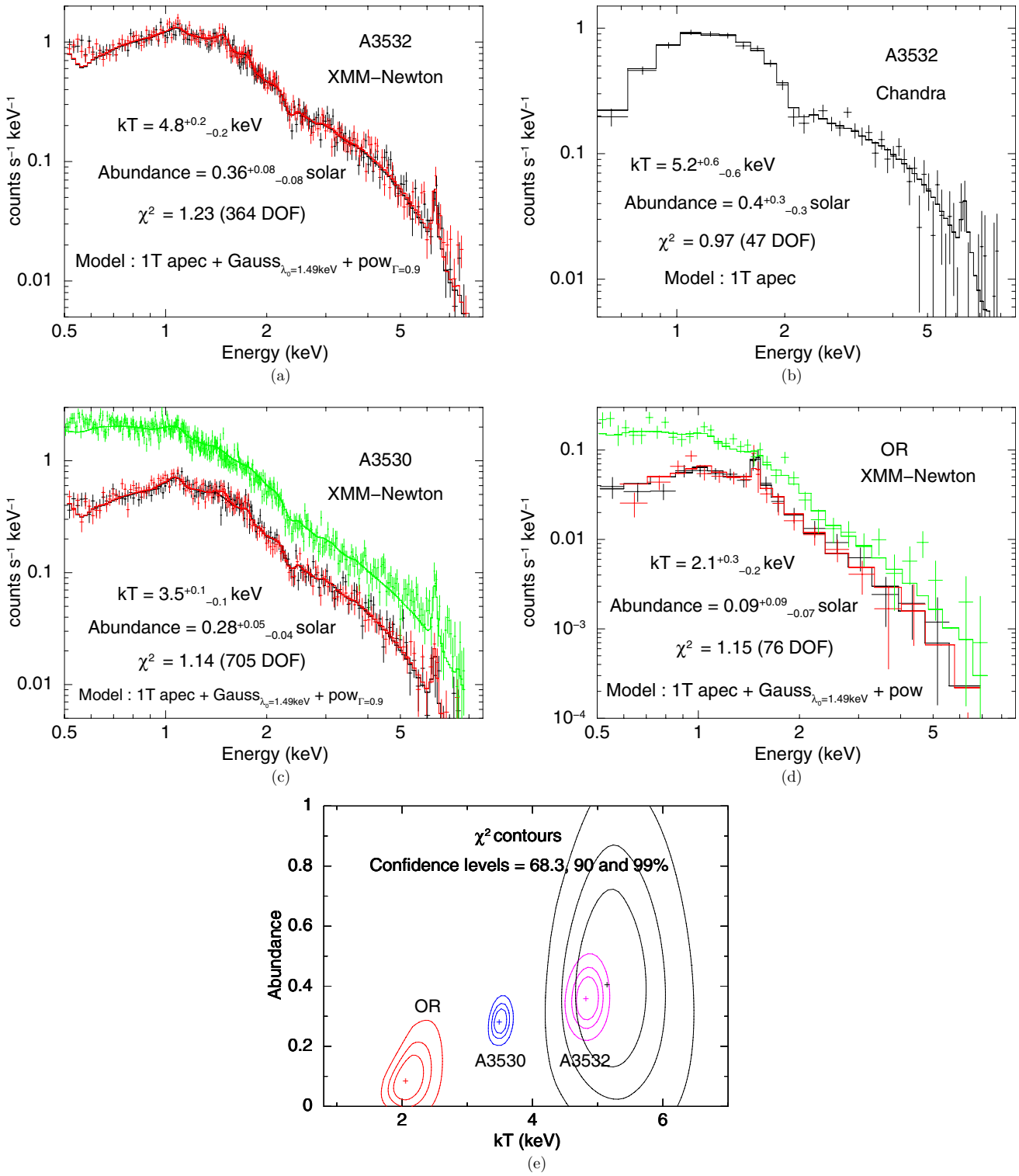

Figure 7. (a)–(c) Average spectra of the clusters A3532 and A3530, and their overlapping region (OR) from *XMM-Newton* MOS1 (black), MOS2 (red), and PN (green) detectors. All the spectra have been fitted with *wabs*apec* model shown as a histogram. Details of the spectral analysis are given in Section 4.2, and the best-fit parameters are shown here as insets. (d) Average spectra of A3532 from *Chandra* data, fitted with the *wabs*apec* model shown as a histogram. (e) The χ^2 contours of the temperature and abundance measurements for the cluster A3532 (pink: *XMM-Newton*; black: *Chandra*) and A3530 (blue: *XMM-Newton*), and the overlapping region (OR) (red: *XMM-Newton*). The confidence levels for the innermost, middle, and outermost contours for each of the four sets of contours are at 68.3%, 90%, and 99%, respectively.

(A color version of this figure is available in the online journal.)

free. To model the residual SP contamination, separate power-law models (see Snowden & Kuntz 2011) were used, and to model the instrumental 1.49 keV Al Kα line, separate Gaussian components for MOS1, MOS2, and PN (see Snowden & Kuntz 2011) were used. The *Chandra* spectrum of A3532 was fitted using only the *wabs*apec* model. The resulting spectra from all detectors, along with the histograms of the best-fit model spectra, are shown in Figures 7(a)–(d). The best-fit values of

Table 3
Best-fit Parameters Obtained from the Spectral Analysis done Using Both *XMM-Newton* and *Chandra* Data for the Cluster A3532, and Using Only *XMM-Newton* Data for the Cluster A3530 and the Overlapping Region (OR) between the Clusters (Section 4.2)

Region	Satellite	kT (keV)	Abundance (Rel. to solar)	*apec* norm. (10^{-3} cm^{-5})	L_X (0.5–8.0 keV) (10^{43} erg s^{-1})	L_X[a] (0.1–2.4 keV) (10^{43} erg s^{-1})	$(\chi^2_\nu)_{min}$ (dof)
A3532	*XMM-Newton*	4.8 ± 0.2	0.36 ± 0.08	16.2 ± 0.4	14.0 ± 0.3	10.2 ± 0.1	1.23(364)
A3532	*Chandra*	$5.2^{+0.6}_{-0.6}$	$0.4^{+0.3}_{-0.3}$	14.6 ± 1.1	13.2 ± 0.6	...	0.97(47)
A3532	*ASCA*[b]	4.4 ± 0.2	...	...	...	12.0 ± 0.4	...
A3530	*XMM-Newton*	3.5 ± 0.1	$0.28^{+0.05}_{-0.04}$	9.9 ± 0.2	7.6 ± 0.1	4.9 ± 0.1	1.13(705)
A3530	*ASCA*[b]	4.1 ± 0.3	...	...	...	6.6 ± 0.3	...
OR	*XMM-Newton*	$2.1^{+0.3}_{-0.2}$	$0.09^{+0.09}_{-0.07}$	1.6 ± 0.2	0.81 ± 0.05	...	1.15(76)

Notes. X-ray luminosities of the two clusters derived in Section 4.3 are given. Results from Ikebe et al. (2002) based on *ASCA* data are also given for comparison. The spectrum for each region is fitted with a single-temperature *apec* model for a fixed Galactic absorption. For the *XMM-Newton* spectral analysis, the residual soft proton contamination and the instrumental Al line at 1.49 keV have been modeled by adding power laws and Gaussians, respectively (separately for MOS1, MOS2, and PN) to the models. Best-fit values for the temperature (kT), elemental abundance relative to the solar values, normalization of the *apec* model, X-ray luminosity (L_X), and minimum reduced χ^2_ν are given along with the degrees of freedom (dof). For the *XMM-Newton* spectral analysis of the cluster A3532, only MOS1 and MOS2 data have been used while for the cluster A3530 and the overlapping region, PN data have also been used.
All errors are quoted at 90% confidence level based on χ^2_{min}+2.71.
[a] The column shows the 0.1–2.4 keV luminosities of A3532 and A3530 obtained by us using *XMM-Newton* data, for a comparison with the results of Ikebe et al. (2002). The values of hydrogen column density and the redshifts have been frozen to the values used by Ikebe et al., although their values, which were used for the rest of the analyses, do not change the results significantly.
[b] The rows show the X-ray temperatures of the hot components and the 0.1–2.4 keV luminosities of A3532 and A3530, obtained by Ikebe et al. (2002) by fitting 2-T thermal plasma model to the *ASCA* spectra of the clusters. The luminosities have been scaled for the currently used value of the Hubble constant (= 70 km s^{-1} Mpc^{-1}).

temperature, abundance, and *apec* normalizations are provided in Table 3.

The confidence contours of the fitted temperatures and abundances, resulting from the spectral analyses at the 68.3%, 90%, and 99% confidence levels are shown in Figure 7(e). It can be seen that the temperatures of the three regions are distinct at the 99% confidence level. The cluster A3532 has the highest temperature (4.8 ± 0.2 keV) and the OR has the lowest temperature ($2.1^{+0.3}_{-0.2}$ keV). The abundance for the cluster A3532 is not distinct from that for the cluster A3530, even at the confidence level of 68.3%. The OR has a distinct abundance and the lowest one (at 90% confidence level) among all the cluster regions. The *Chandra* and *XMM-Newton* results for A3532 are in good agreement, although results from *Chandra* have larger errors.

4.3. X-Ray Luminosity Estimates

X-ray luminosities of A3532 and A3530 in the energy range of 0.5–8.0 keV were estimated using the *XMM-Newton* data (for A3532, using *Chandra* data as well) from the flux values obtained from the spectral analysis of these regions described in Section 4.2. The fluxes (F_X) were estimated by convolving the model used in Section 4.2 with the *XSPEC* convolution model *cflux* after freezing the *apec* normalization. The X-ray luminosities (L_X) were derived from the fluxes using the formula

$$L_X = 4\pi D_L^2 F_X, \quad (1)$$

where D_L is the luminosity distance to the source. The values of luminosities (L_X) derived using this relation for the two clusters are given in Table 3. The 0.1–2.4 keV luminosities have also been estimated for the two clusters for comparison with values obtained by Ikebe et al. (2002) by fitting 2-T thermal plasma models to the *ASCA* spectra of the clusters. The luminosities obtained by Ikebe et al. have been scaled for the currently used value of the Hubble constant, i.e., 70 km s^{-1} Mpc^{-1}. For the 0.1–2.4 keV luminosity estimates obtained by us, the values of the hydrogen column density and the redshifts have been frozen to the values used by Ikebe et al. for consistency. However, 2-T thermal plasma models could not be fitted to our spectra as the normalizations of the second *apec* components were negligibly small. We have, therefore, used only the 1-T *apec* models throughout our analyses. The 0.1–2.4 keV luminosities obtained by us are only slightly lower than those obtained by Ikebe et al. (2002), possibly due to the different spectral models used for the two analyses. These results have also been listed in Table 3.

Table 4
Results of β-model Fitting of the Surface Brightness Profiles of the Clusters A3532 and A3530 and Their Bolometric X-Ray Luminosities

Cluster	β	r_c (10^{-2} Mpc)	F_X^b (10^{-11} erg cm^{-2} s^{-1})	L_X^b (10^{44} erg s^{-1})
A3532	0.41 ± 0.01	8.1 ± 0.5	3.4 ± 0.3	2.5 ± 0.2
A3530	0.47 ± 0.01	9.7 ± 0.5	1.3 ± 0.2	0.9 ± 0.1

Notes. Errors are quoted at 68% confidence level (1σ) based on χ^2_{min}+1.00. F_X^b = bolometric X-ray flux, $\beta = -1/3$(slope−0.5), and r_c = core radius.

We have also estimated the bolometric X-ray luminosities of the clusters A3532 and A3530. The average count rates of the two clusters were obtained by fitting their 0°–360° surface brightness profiles with the β-model. These count rates were converted to fluxes in the 0.01–100 keV energy band, by using the HEASARC tool Web Portable, Interactive, Multi-Mission Simulator, from which the bolometric X-ray luminosities were estimated by using Equation (1). The results obtained from the β-model fitting along with the estimated X-ray bolometric luminosities of A3532 and A3530 have been given in Table 4. By analyzing the X-ray bolometric luminosities and temperatures of 274 clusters and 66 groups of galaxies, Xue & Wu (2000) obtained their L_X–kT relations as $L_X = 10^{-0.032\pm0.065} T^{2.79\pm0.08}$

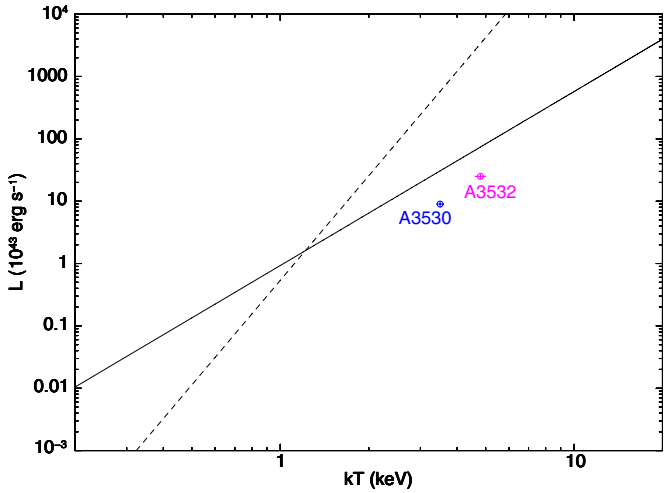

Figure 8. L_X–kT relations of rich clusters (solid line) and isolated groups of galaxies (dashed line), obtained by Xue & Wu (2000). The positions of A3532 and A3530 have also been shown.

(A color version of this figure is available in the online journal.)

and $L_X = 10^{-0.27\pm0.05}T^{5.57\pm1.79}$, for rich clusters and isolated groups of galaxies, respectively, where L_X is in the units of 10^{43} erg s^{-1}, and T is in the units of keV. Figure 8 shows these relations using lines on a log–log plot along with the positions of A3532 and A3530. The two clusters lie very close to the line for the rich clusters of galaxies with only slightly higher temperatures.

4.4. Radial Profiles of Thermodynamic Quantities Based on Azimuthally Averaged Spectra

We have produced the azimuthally averaged profiles of temperature, density, entropy, and pressure by extracting spectra in eight circular annuli in each of the clusters A3532 and A3530 using *XMM-Newton* data. For the cluster A3532, *Chandra* data were also used for making these profiles. As *Chandra* did not cover the full extent of the three outermost annuli in A3532, only the first five annuli were used for *Chandra* data. The annuli centers were at the peak of the X-ray emission of each cluster, and the radius of the nth annulus was $n \times 75''$ for both clusters. All spectra were extracted in the 0.5–8.0 keV energy band.

4.4.1. Two-dimensional Projected Profiles

To determine the 2D profiles, we used the same method as given in Section 4.2 for spectral analysis. As no significant variations were seen in the elemental abundances of the annuli belonging to A3532, their values were frozen to that obtained in Section 4.2, i.e., 0.36 times the solar value ($Z_\odot$) (Table 3). In A3530, the elemental abundance was found to be significantly varying, therefore, for the spectral analysis of the annuli belonging to A3530, the elemental abundance was kept as a free parameter. We have verified for both clusters that while results do not change significantly for a free or frozen elemental abundance, their errors decrease slightly for a frozen abundance. For *XMM-Newton* spectra, the residual SP contamination and instrumental Al lines were modeled by adding power laws and Gaussian components to the models as was also done in Section 4.2. Projected profiles of temperature (kT), density (n_e), entropy (S), and pressure (P) were produced and are shown as the left-hand side images in Figures 9 and 10. The temperature profiles were obtained as a direct result of the spectral analyses and are shown in Figures 9(a) and 10(a) for A3532 and A3530, respectively. To derive the electron density n_e, we used the *apec* normalizations, $K = 10^{-14}\mathrm{EI}/(4\pi[D_A(1+z)]^2)$, where EI is the emission integral $\int n_e n_p dV$. By assuming, $n_p = 0.855n_e$ (Henry et al. 2004) and a constant density within each spherical shell, we obtain, $\mathrm{EI} = 0.855n_e^2V$, where V is the volume of the spherical shell ($= 4\pi(r_o^3 - r_i^3)$, where r_o and r_i are the radii of the outer and inner annuli forming the shell). The resulting density profiles are shown in Figures 9(c) and 10(c), for A3532 and A3530, respectively. The entropy (S) and the electron pressure (P) are obtained from the relations $S = kTn_e^{-2/3}$ and $P = n_e kT$, respectively (Gitti et al. 2010). The resulting entropy profiles for A3532 and A3530 are shown in Figures 9(e) and 10(e), and the pressure profiles are shown in Figures 9(g) and 10(g), respectively. The values of all the thermodynamic quantities for each of the annuli are tabulated in Tables 5 and 6 for A3532 and A3530, respectively. The temperature profiles obtained using *XMM-Newton* data show low temperatures in the innermost annuli of both the clusters. For the rest of the annuli in A3532, temperature is almost a constant, whereas for A3530, the temperature profile shows a gradual decrease outward. The density, entropy, and pressure profiles of both the clusters show an average decrease, increase, and decrease, respectively, from the innermost to the outermost annulus. The projected profile of the elemental abundance in A3532 is shown in Figure 9(i), and due to large errors, does not show significant variations in the values obtained for different annuli. The elemental abundance in A3530 shows a gradual decrease from the innermost to the outermost annulus (Figure 10(i)), which indicates an enrichment of the ICM toward the center of the cluster. The errors in the abundance profile of A3532 obtained using *XMM-Newton* spectra are much larger than those for A3530. This is because only MOS spectra were used for A3532 while both MOS and PN spectra were used for A3530. All the profiles of thermodynamic quantities obtained using *Chandra* data are consistent with those obtained using *XMM-Newton* data.

4.4.2. Deprojected Profiles

To get a better idea of the variations in the thermodynamic quantities which may get smoothed out due to projection effects, we carried out a deprojection analysis on the annuli described in Section 4.4.1. For this purpose, we used the *XSPEC projct* model, which can estimate the parameters in 3D space from the 2D projected spectra of annular ellipsoidal shells, along with the *wabs*apec* model. As the elemental abundances for all the annuli belonging to A3532 and A3530 did not show significant variations, their values were frozen to 0.36 and 0.28 times the solar value ($Z_\odot$), respectively. For *XMM-Newton* spectra, the residual SP contamination and instrumental Al lines were modeled by adding power laws and Gaussian components to the models as was also done in Section 4.2. Note that, as the *projct* model requires all the spectra belonging to the same annulus to be part of the same group, for each annulus a single power law and Gaussian were used for all MOS1, MOS2, and PN detectors. Electron density (n_e), entropy (S), and electron pressure (P) have been calculated using the same relations as given in Section 4.4.1. The resulting deprojected profiles of temperature, density, entropy, and pressure obtained for A3532 and A3530 are shown plotted on the right-hand sides of Figures 9 and 10, and listed in Tables 7 and 8, respectively.

The deprojected profiles of both clusters have errors larger than the projected profiles. The *XMM-Newton* temperature profiles of the clusters A3532 and A3530 do not change

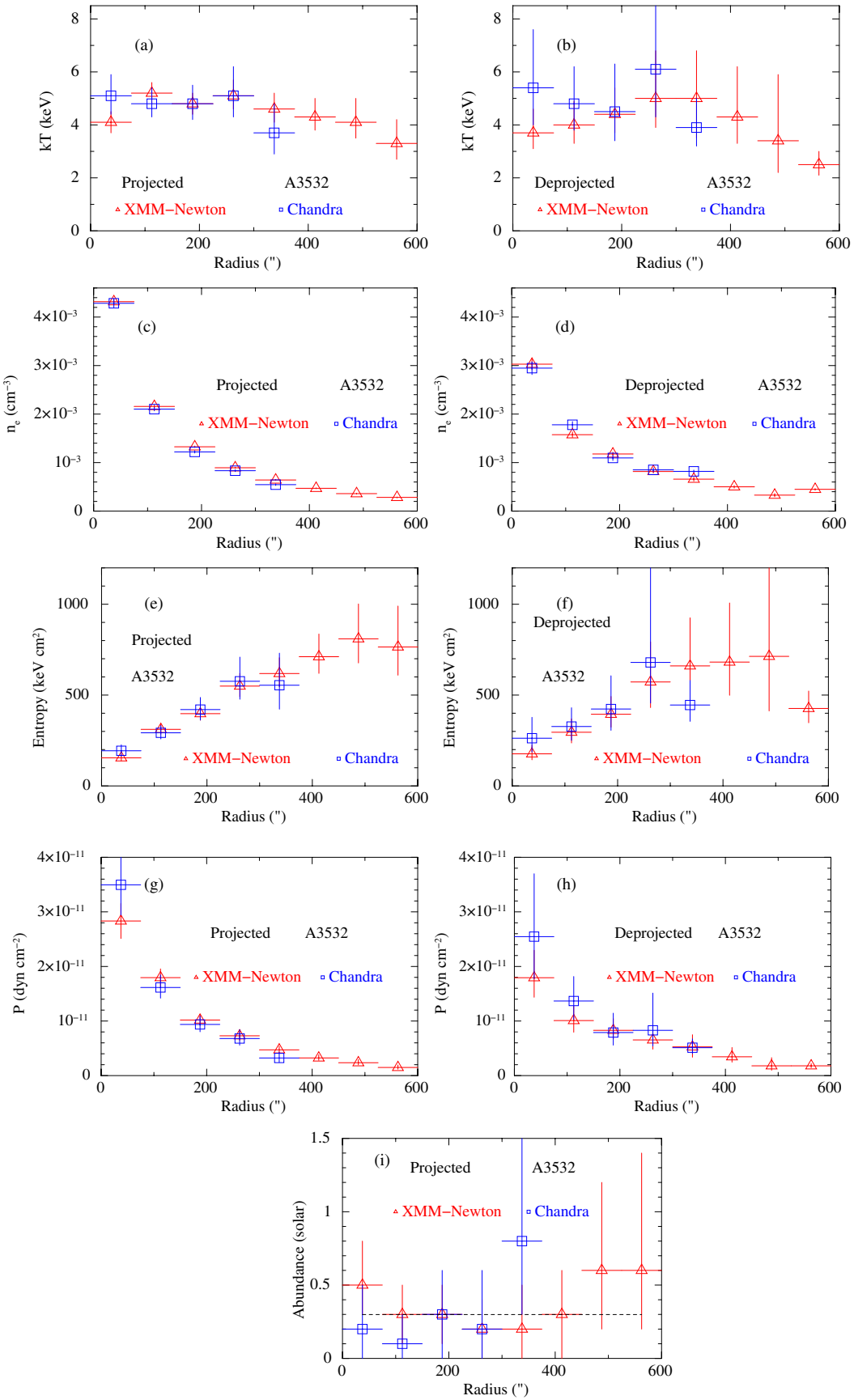

Figure 9. (a)–(h) Projected and deprojected temperature (kT), electron density (n_e), entropy (S), and pressure (P) profiles obtained from the spectral analysis of the *XMM-Newton* MOS spectra from eight circular annuli (red points) and *Chandra* spectra from five circular annuli (blue points) in the cluster A3532. The value of elemental abundance was frozen to 0.36 times the solar value. (i) The abundance profile of A3532 from projected spectral analysis, after freeing the abundance parameter. The details of the projected and deprojected spectral analysis are given in Sections 4.4.1 and 4.4.2, respectively.

(A color version of this figure is available in the online journal.)

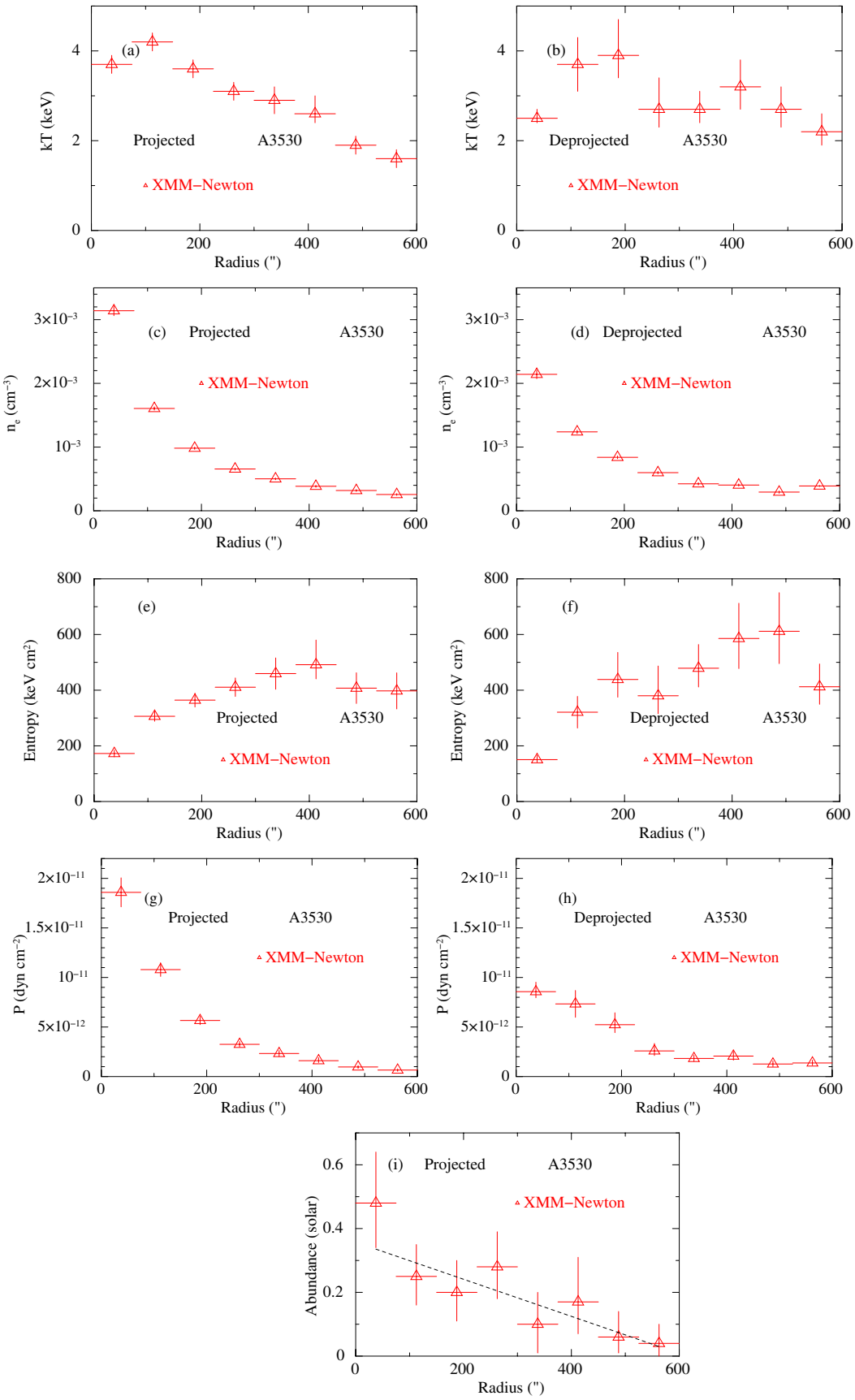

Figure 10. (a)–(h) Projected and deprojected temperature (kT), electron density (n_e), entropy (S), and pressure (P) profiles obtained from the spectral analysis of the *XMM-Newton* (MOS+PN) spectra from eight circular annuli in the cluster A3530. (i) The abundance profile of A3530 from projected spectral analysis. For the deprojected spectral analysis, the value of elemental abundance was frozen to 0.28 times the solar value. The details of the projected and deprojected spectral analysis are given in Sections 4.4.1 and 4.4.2, respectively.

(A color version of this figure is available in the online journal.)

Table 5
Best-fit Parameters Obtained from the Spectral Analysis of Eight Circular Annuli in the Cluster A3532 using *XMM-Newton* MOS1 and MOS2 Data and of Five Circular Annuli Using *Chandra* Data

Data	Annulus Number	kT (keV)	n_e (10^{-4} cm^{-3})	P (10^{-12} dyn cm^{-2})	S (keV cm^2)
XMM-Newton	1	4.1 ± 0.4	43.2 ± 0.7	$28.3^{+3.2}_{-5.5}$	155 ± 17
	2	5.2 ± 0.4	21.6 ± 0.3	$18.0^{+1.6}_{-2.0}$	311 ± 26
	3	4.8 ± 0.4	13.3 ± 0.2	$10.2^{+1.0}_{-1.4}$	398 ± 36
	4	$5.1^{+0.6}_{-0.5}$	8.9 ± 0.1	$7.3^{+1.0}_{-1.2}$	550^{+69}_{-59}
	5	$4.6^{+0.6}_{-0.5}$	6.4 ± 0.1	$4.7^{+0.7}_{-0.8}$	619^{+87}_{-74}
	6	$4.3^{+0.7}_{-0.5}$	4.7 ± 0.1	$3.2^{+0.6}_{-0.8}$	711^{+125}_{-92}
	7	$4.1^{+0.9}_{-0.6}$	3.6 ± 0.1	$2.4^{+0.6}_{-0.8}$	810^{+192}_{-133}
	8	$3.3^{+0.9}_{-0.6}$	2.8 ± 0.1	$1.5^{+0.5}_{-0.4}$	765^{+225}_{-156}
Chandra	1	$5.1^{+0.8}_{-0.7}$	42.8 ± 0.9	$35.0^{+6.2}_{-5.5}$	193^{+33}_{-29}
	2	$4.8^{+0.6}_{-0.5}$	21.0 ± 0.4	$16.1^{+2.3}_{-2.0}$	292^{+40}_{-34}
	3	$4.8^{+0.7}_{-0.6}$	12.2 ± 0.2	$9.4^{+1.5}_{-1.3}$	420^{+67}_{-58}
	4	$5.1^{+1.1}_{-0.8}$	8.3 ± 0.2	$6.8^{+1.6}_{-1.2}$	576^{+133}_{-99}
	5	$3.7^{+1.1}_{-0.8}$	5.5 ± 0.2	$3.2^{+1.1}_{-0.8}$	554^{+177}_{-132}

Notes. The spectra for all the annuli were fitted using the model *wabs*apec* for a fixed value of Galactic absorption and with elemental abundances frozen to 0.36 times the solar value. For *XMM-Newton* spectra, the residual soft proton contamination and the instrumental Al line at 1.49 keV have been modeled by adding power laws and Gaussians, respectively (separately for MOS1 and MOS2) to the models. Annulus number represents the position of the annulus from the innermost to the outermost annuli in increasing order. Values of temperature (kT), electron density (n_e), pressure (P), and entropy (S) are listed. All errors are quoted at 90% confidence level based on χ^2_{min}+2.71.

Table 6
Best-fit Parameters Obtained from the Spectral Analysis of Eight Circular Annuli in the Cluster A3530 Using *XMM-Newton* Data

Annulus Number	kT (keV)	Abundance (Relative to Solar)	n_e (10^{-4} cm^{-3})	P (10^{-12} dyn cm^{-2})	S (keV cm^2)
1	3.7 ± 0.2	$0.5^{+0.2}_{-0.1}$	31.4 ± 0.8	18.6 ± 1.5	172 ± 12
2	4.2 ± 0.2	0.3 ± 0.1	16.1 ± 0.3	10.8 ± 0.7	306 ± 18
3	3.6 ± 0.2	0.2 ± 0.1	9.8 ± 0.2	5.7 ± 0.4	364 ± 25
4	3.1 ± 0.2	0.3 ± 0.1	6.6 ± 0.2	3.3 ± 0.3	411 ± 33
5	2.9 ± 0.3	0.1 ± 0.1	5.0 ± 0.1	2.3 ± 0.3	460 ± 56
6	$2.6^{+0.4}_{-0.2}$	0.2 ± 0.1	3.8 ± 0.2	$1.6^{+0.3}_{-0.2}$	491^{+89}_{-51}
7	1.9 ± 0.2	0.1 ± 0.1	3.2 ± 0.1	1.0 ± 0.1	407 ± 55
8	1.6 ± 0.2	$0.04^{+0.06}_{-0.04}$	2.6 ± 0.1	0.7 ± 0.1	397 ± 65

Notes. The spectra for all the annuli were fitted using the model *wabs*apec* for a fixed value of Galactic absorption. The residual soft proton contamination and the instrumental Al line at 1.49 keV have been modeled by adding power laws and Gaussians, respectively (separately for MOS1, MOS2, and PN) to the models. Annulus number represents the position of the annulus from the innermost to the outermost annuli in increasing order. Values of temperature (kT), abundance, electron density (n_e), pressure (P), and entropy (S) are listed. All errors are quoted at 90% confidence level based on χ^2_{min}+2.71.

significantly and are almost constant from the innermost to the outermost annulus, except for the innermost annulus of A3530, which shows a significantly lower temperature. On average, the density, entropy, and pressure profiles of both the clusters show a gradual decrease, increase, and decrease, respectively, from the innermost to the outermost annulus, as in their projected profiles. Results from *Chandra* and *XMM-Newton* for the cluster A3532 are in good agreement with each other. However, the errors from *Chandra* data are much larger than those from *XMM-Newton*, as also observed for the projected profiles. The projected and deprojected profiles of both the clusters do not seem to be significantly different, except for a few anomalies. The density values in the inner annuli of both the clusters, obtained from the projected spectral analysis, are higher than those from the deprojected spectral analysis. Similarly, the pressure values in the inner annuli of both the clusters, obtained from the *XMM-Newton* projected spectral analysis, are higher than those from the deprojected spectral analysis.

4.5. Spectrally Determined 2D Projected Thermodynamic Maps at a Higher Resolution

The 2D projected temperature, density, entropy, and pressure maps for the combined system of the A3532 and A3530 clusters have also been made, using *XMM-Newton* spectra from a total of 77 box-shaped regions. As *Chandra* data (available only for the A3532 cluster) had large errors (evident in Sections 4.2, 4.4.1, and 4.4.2), we have not used the *Chandra* data in this section. Out of the 77 box regions, 41 boxes were from A3532 and 37 were from A3530, with one box in common. An adaptive approach was followed for choosing the sizes of the boxes, so as to get sufficient counts in each region. Large size boxes ($\sim 7\farcm7 \times 3\farcm8$)

Table 7
Best-fit Parameters Obtained from the Deprojected Spectral Analysis of Eight Circular Annuli in the Cluster A3532 Using *XMM-Newton* MOS1 and MOS2 Data and of Five Circular Annuli Using *Chandra* Data

Data	Annulus Number	kT (keV)	n_e (10^{-4} cm^{-3})	P (10^{-12} dyn cm^{-2})	S (keV cm^2)
XMM-Newton	1	$3.7^{+0.9}_{-0.6}$	30.3 ± 1.1	$17.9^{+5.0}_{-3.6}$	177^{+47}_{-33}
	2	$4.0^{+0.9}_{-0.7}$	15.8 ± 0.6	$10.1^{+2.6}_{-2.1}$	295^{+74}_{-59}
	3	$4.4^{+1.0}_{-0.7}$	11.8 ± 0.4	$8.3^{+2.1}_{-1.6}$	395^{+98}_{-71}
	4	$5.0^{+1.8}_{-1.1}$	8.2 ± 0.3	$6.5^{+2.6}_{-1.7}$	572^{+221}_{-141}
	5	$5.0^{+1.8}_{-1.5}$	6.6 ± 0.4	$5.3^{+2.2}_{-1.9}$	661^{+265}_{-225}
	6	$4.3^{+1.9}_{-1.0}$	5.0 ± 0.3	$3.4^{+1.7}_{-1.0}$	682^{+325}_{-183}
	7	$3.4^{+2.5}_{-1.2}$	3.3 ± 0.3	$1.8^{+1.5}_{-0.8}$	713^{+573}_{-301}
	8	$2.5^{+0.5}_{-0.4}$	4.5 ± 0.2	$1.8^{+0.4}_{-0.4}$	426^{+96}_{-79}
Chandra	1	$5.4^{+2.2}_{-1.4}$	29.5 ± 1.3	$25.5^{+11.2}_{-7.7}$	263^{+115}_{-76}
	2	$4.8^{+1.4}_{-1.0}$	17.8 ± 0.7	$13.7^{+4.5}_{-3.4}$	327^{+104}_{-76}
	3	$4.5^{+1.8}_{-1.1}$	11.0 ± 0.5	$7.9^{+3.5}_{-2.3}$	423^{+183}_{-117}
	4	$6.1^{+4.7}_{-1.8}$	8.5 ± 0.4	$8.3^{+6.8}_{-2.9}$	680^{+547}_{-224}
	5	$3.9^{+1.1}_{-0.7}$	8.2 ± 0.3	$5.1^{+1.6}_{-1.1}$	445^{+135}_{-90}

Notes. The spectra for all the annuli were fitted using the model *wabs*apec* for a fixed value of Galactic absorption and with elemental abundances frozen to 0.36 times the solar value. For *XMM-Newton* spectra, the residual soft proton contamination and the instrumental Al line at 1.49 keV have been modeled by adding power laws and Gaussians, respectively, to the models. Annulus number represents the position of the annulus from the innermost to the outermost annuli in increasing order. Values of temperature (kT), electron density (n_e), pressure (P), and entropy (S) are listed. All errors are quoted at 90% confidence level based on $\chi^2_{\rm min}$+2.71.

Table 8
Best-fit Parameters Obtained from the Deprojected Spectral Analysis of Eight Circular Annuli in the Cluster A3530 Using *XMM-Newton* Data

Annulus Number	kT (keV)	n_e (10^{-4} cm^{-3})	P (10^{-12} dyn cm^{-2})	S (keV cm^2)
1	$2.5^{+0.2}_{-0.1}$	21.4 ± 0.7	$8.6^{+1.0}_{-0.6}$	150^{+15}_{-9}
2	3.7 ± 0.6	12.4 ± 0.3	7.3 ± 1.4	321 ± 57
3	$3.9^{+0.8}_{-0.5}$	8.4 ± 0.2	$5.2^{+1.2}_{-0.8}$	438^{+97}_{-64}
4	$2.7^{+0.7}_{-0.4}$	6.0 ± 0.2	$2.6^{+0.8}_{-0.5}$	380^{+107}_{-65}
5	$2.7^{+0.4}_{-0.3}$	4.2 ± 0.2	$1.8^{+0.4}_{-0.3}$	479^{+85}_{-67}
6	$3.2^{+0.6}_{-0.5}$	4.0 ± 0.2	$2.1^{+0.5}_{-0.4}$	586^{+127}_{-108}
7	$2.7^{+0.5}_{-0.4}$	2.9 ± 0.2	1.3 ± 0.3	611^{+139}_{-116}
8	$2.2^{+0.4}_{-0.3}$	3.9 ± 0.1	$1.4^{+0.3}_{-0.2}$	412^{+82}_{-63}

Notes. The spectra for all the annuli were fitted using the model *wabs*apec* for a fixed value of Galactic absorption and with elemental abundances frozen to 0.28 times the solar value. The residual soft proton contamination and the instrumental Al line at 1.49 keV have been modeled by adding power laws and Gaussians, respectively, to the models. Annulus number represents the position of the annulus from the innermost to the outermost annuli in increasing order. Values of temperature (kT), electron density (n_e), pressure (P), and entropy (S) are listed. All errors are quoted at 90% confidence level based on $\chi^2_{\rm min}$+2.71.

for the outermost parts, small size boxes ($\sim 1\farcm9 \times 1\farcm9$) for the innermost brightest parts, and medium sized boxes ($\sim 1\farcm9 \times 3\farcm8$) for the regions in between were selected in order to get more than 700 total counts from all three detectors in each box. Spectra from all boxes were fitted using *wabs*apec* model with fixed Galactic absorption. As described in Section 4.2, the residual SP contamination and instrumental Al lines were modeled by adding power laws and Gaussian components to the models. Because of the poor statistics and large errors in the abundance values, the elemental abundances for all the box regions were fixed to the average abundance value of the cluster (see Section 4.2) to which the box belonged, i.e., 0.36 and 0.28 times the solar value ($Z_\odot$) for the boxes belonging to A3532 and A3530, respectively. The electron density, entropy, and electron pressure were calculated using the same relations as in Section 4.4.1. Spherical geometry was assumed for the volume calculation. All 77 box regions were assumed to be projections of parts of spherical shells (centered at the X-ray intensity peak of the cluster to which the box belongs) with inner and outer radii ($R_{\rm in}$, $R_{\rm out}$) equal to the smallest and largest distance from the center of their respective spheres. The volume for each box region was estimated as $D_A^3 \Omega(\theta_{\rm out}^2 - \theta_{\rm in}^2)^{1/2}$ (Henry et al. 2004; Ehlert et al. 2011), where D_A is the angular diameter distance of the cluster to which the box belongs and Ω is the solid angle subtended by the box. $\theta_{\rm in}$ and $\theta_{\rm out}$ are equal to the distances $R_{\rm in}$ and $R_{\rm out}$ expressed in angular units, respectively. For a box region common to both A3532 and A3530 an average of results from the two observations was used.

The temperature, density, entropy, and pressure maps produced are shown in Figures 11(a), 11(b), 12(a), and 12(b), respectively. The temperature in both clusters appears to decrease as we move outward from the center. However, A3532 shows a lot of anisotropic variations in the temperature, especially in its central parts, though the statistical significance is low. Both density and pressure maps show a peak at the center of the clusters followed by an almost uniform decrease outward. The entropy maps of both clusters show the presence of a few high entropy regions in their outer parts while almost a constant entropy is observed in their inner parts. The OR between the two clusters does not show the presence of high temperature or high entropy, as would have been expected if an active merger was taking place between the two clusters. We have also made an estimate of the density (n_e in the OR by using the *apec* normalization obtained in Section 4.2. For volume calculation, we assumed a prolate ellipsoid made using the ellipse used in Section 4.2 for the OR. We obtained a density of $(6.4 \pm 0.4) \times 10^{-4}$ cm^{-3} for the OR, which is consistent with its value from Figure 11(b).

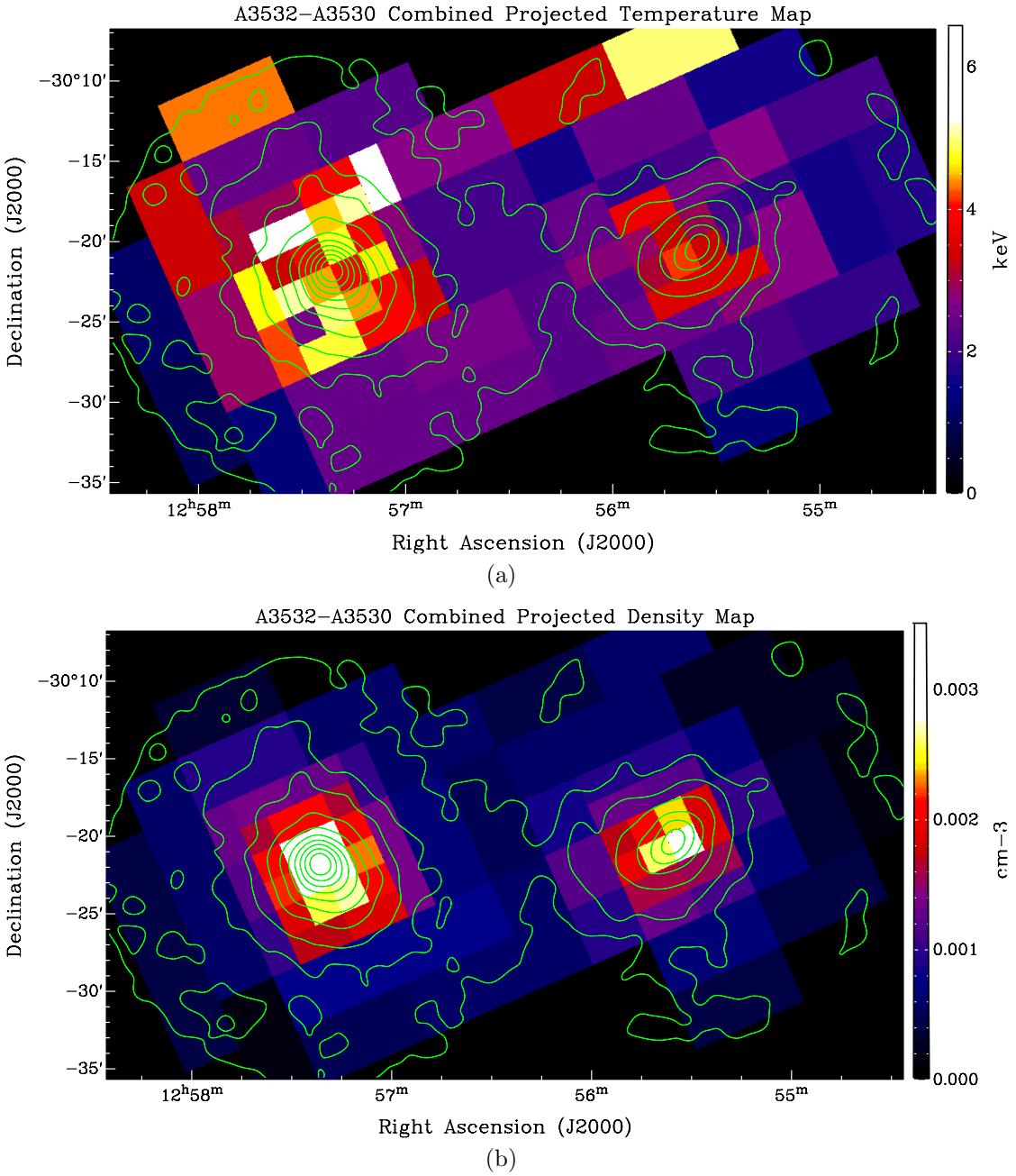

Figure 11. (a) Projected temperature (kT) map from 77 box regions in the clusters A3532 and A3530 using *XMM-Newton* data. The scale is expressed in keV units and is shown in the bar alongside. (b) Projected density (n_e) map from 77 box regions in the clusters A3532 and A3530 using *XMM-Newton* data. The scale is expressed in the units of cm^{-3} and is shown in the bar alongside. X-ray surface brightness contours, with levels the same as in Figure 1, have been overlaid on both the figures. Details of the spectral fittings are provided in Section 4.5.

(A color version of this figure is available in the online journal.)

4.6. Cooling Time

A commonly used relation for estimating the cooling time of a cluster from Sarazin (1988), is as follows:

$$t_{\rm cool} = 8.5 \times 10^{10}\ {\rm yr} \left[\frac{n}{10^{-3}\ {\rm cm}^{-3}}\right]^{-1} \left[\frac{T_{\rm g}}{10^{8}\ {\rm K}}\right]^{1/2}. \quad (2)$$

Using this relation and the central gas temperatures ($T_{\rm g}$) and densities (n) (derived from the deprojection analysis in Section 4.4.2, the cooling times estimated for both A3532 and A3530 (= 1.8×10^{10} yr and 1.7×10^{10} yr, respectively) seem to be longer than the Hubble time ($\sim 1.35 \times 10^{10}$ yr). Note that the innermost annuli in Section 4.4.2 have radii equal to 75″ (∼80 kpc). It should also be noted that the above relation is derived by assuming thermal bremsstrahlung as the only cooling mechanism. However, additional cooling by line emission may result in a smaller value of the cooling time. Using the continuum and line emissivity relations given in Sarazin (1988), the cooling time of A3530 ($\sim 1.02 \times 10^{10}$ yr) seems to be slightly lower while that of A3532 ($\sim 1.26 \times 10^{10}$ yr) seems to be very close to the Hubble time. A discussion regarding the possibility of cool cores in the cluster pair, based on the results obtained in this section along with some other results, is given in Section 5.

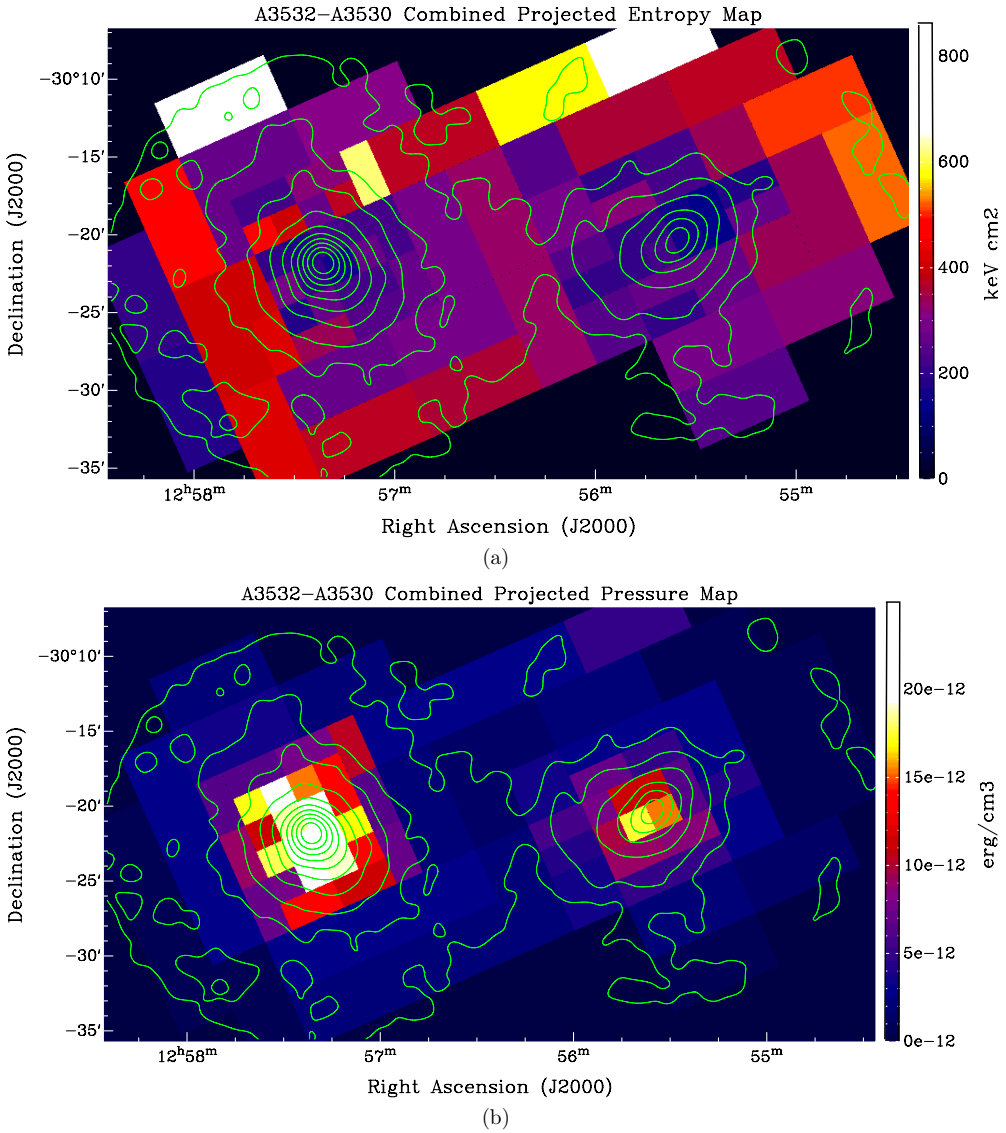

Figure 12. (a) Projected entropy map from 77 box regions in the clusters A3532 and A3530 using *XMM-Newton* data. The scale is expressed in units of keV cm^2 and is shown in the bar alongside. (b) Projected pressure map from 77 box regions in the clusters A3532 and A3530 using *XMM-Newton* data. The scale is expressed in the units of erg cm^{-3} and is shown in the bar alongside. X-ray surface brightness contours, with levels the same as in Figure 1, have been overlaid on both the figures. Details of the spectral fittings are provided in Section 4.5.

(A color version of this figure is available in the online journal.)

4.7. Gas Mass Estimation

We have estimated the gas masses for A3532 and A3530 by using the gas density profiles obtained in Sections 4.4.1 and 4.4.2. The projected and deprojected gas density profiles for both clusters were fitted using a β-model, i.e.,

$$n_{\rm e}(r) = n_{\rm e}\,(0)\left(1+\frac{r^2}{r_{\rm c}^2}\right)^{(3/2)\beta}, \qquad (3)$$

where $n_{\rm e}(0)$ is the central density and $r_{\rm c}$ is the core radius. The gas masses $M_{\rm gas}(r)$ out to radii 0.5 Mpc and 1 Mpc for the two clusters were obtained by using the following formula (see Donnelly et al. 2001):

$$M_{\rm gas}(r) = 4\pi\rho_0\int_0^r s^2\left[1+\left(\frac{s}{r_{\rm c}}\right)^2\right]^{(3/2)\beta} ds, \qquad (4)$$

where $\rho_0 = \mu n_{\rm e}(0) m_{\rm p}$, $m_{\rm p}$ is the mass of a proton, and $\mu = 0.609$ is the average molecular weight for a fully ionized gas (Gu et al. 2010). The values of β, $r_{\rm c}$, ρ_0, and $M_{\rm gas}$ based on fitting the density profiles with the above model are listed in Table 9. the results obtained from both projected and deprojected analysis show A3532 to be marginally more massive than A3530.

4.8. Galaxy Velocity Distribution and Virial Mass

The presence of substructures and mergers in clusters of galaxies often results in multimodal and asymmetric/non-Gaussian velocity distributions. Therefore, to look for the presence of substructures and mergers in A3532 and A3530, we used the galaxy velocity samples from Cristiani et al. (1987) and Bardelli et al. (2001), respectively. As Bardelli et al. have given velocity information for a large number of galaxies located in the core of the SSC, the galaxies selected for A3530 might also have included background and foreground galaxies. Therefore, upper and lower velocity thresholds of 15,000

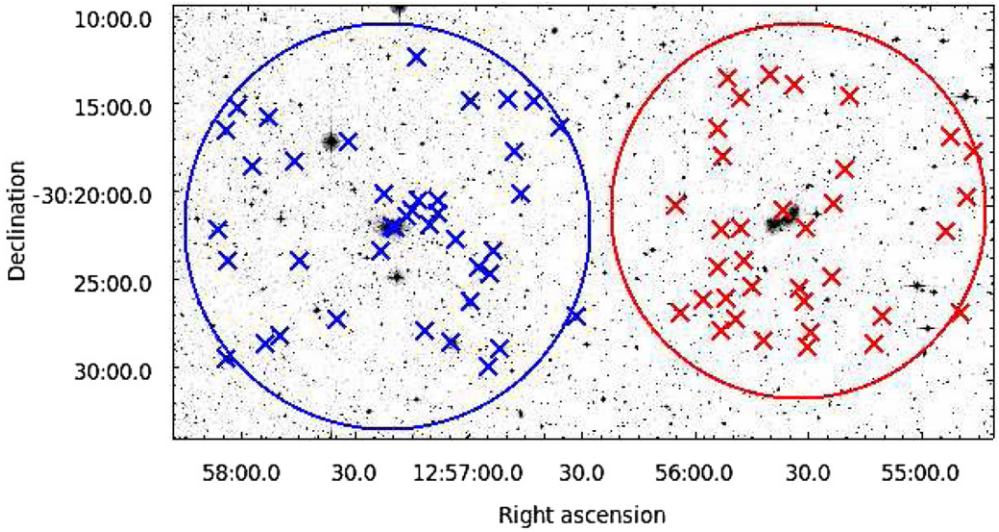

Figure 13. Positions of the galaxies used for the analysis in Section 4.8 marked on the SuperCOSMOS image. The circles mark the 0.5 R_{200} radii of the clusters and the crosses mark the positions of the galaxies. Blue and red colors have been used for A3532 and A3530, respectively.

(A color version of this figure is available in the online journal.)

Table 9
Mass of Hot Gas for the Clusters A3532 and A3530 Obtained by Fitting β-models to the Projected and Deprojected Density Profiles Obtained in Sections 4.4.1 and 4.4.2, Respectively

Spectral Analysis	Cluster	Data	β	r_c (kpc)	ρ_0 (10^{13} $M_\odot$ Mpc^{-3})	r (Mpc)	$M_{\rm gas}(r)$ (10^{13} $M_\odot$)
Projected	A3532	*XMM-Newton*	0.68 ± 0.01	77 ± 3	10.3 ± 0.1	0.5	0.70 ± 0.04
						1.0	2.3 ± 0.2
		Chandra	0.68 ± 0.03	71 ± 1	10.6 ± 0.2	0.5	0.6 ± 0.1
						1.0	2.1 ± 0.3
	A3530	*XMM-Newton*	0.64 ± 0.01	67 ± 2	8.0 ± 0.1	0.5	0.53 ± 0.03
						1.0	1.8 ± 0.1
Deprojected	A3532	*XMM-Newton*	0.54 ± 0.03	71 ± 9	7.1 ± 0.2	0.5	0.7 ± 0.1
						1.0	2.6 ± 0.5
		Chandra	0.52 ± 0.08	72 ± 2	7.1 ± 0.3	0.5	0.7 ± 0.2
						1.0	2.8 ± 1.2
	A3530	*XMM-Newton*	0.54 ± 0.02	73 ± 8	5.1 ± 0.1	0.5	0.5 ± 0.1
						1.0	2.0 ± 0.3

Note. Errors are quoted at 68% confidence level (1σ) based on $\chi^2_{\rm min}$+1.00.

and 17,600 km s^{-1}, respectively, were applied to the sample of Bardelli et al. In addition, to avoid overlaps, galaxies only within 0.5 R_{200} circles,[4] centered on the X-ray surface brightness peaks were used for this analysis (see Figure 13), for both the clusters. This led to 40 galaxies with velocity information in A3532 and 35 galaxies in A3530. The histograms of galaxy velocity distributions of the two clusters overlaid with their Gaussian fits are shown in Figure 14. The bin size used for both the clusters was 350 km s^{-1}. A single Gaussian can be fitted to the velocity histogram of each of the two clusters. Therefore, neither cluster shows the presence of substructures in its optical redshift distribution. This result is in agreement with the findings of Pimbblet (2008) for the cluster A3532, based on the Dressler & Shectman (1988) δ-test. Based on Gaussian fits, we obtain the average radial velocities of A3532 and A3530 as 16211 ± 159 km s^{-1} and 16213 ± 246 km s^{-1}, respectively, which translate to average redshifts of 0.0556 ± 0.0005 and 0.0556 ± 0.0009, respectively. The result, therefore, strengthens the argument that the two clusters are at the same distance and much closer to each other than previously thought and, therefore, have a very high probability of tidally interacting with each other.

We have also estimated the virial masses of the two clusters by using these galaxy velocity samples and the relation given by Beers et al. (1982):

$$M_{\rm virial} = \frac{3\pi}{G}\sigma_{\rm r}^2 \left\langle \frac{1}{r_{\rm p}} \right\rangle^{-1}, \quad (5)$$

where $\sigma_{\rm r}$ is the velocity dispersion along the line of sight and $\langle 1/r_{\rm p} \rangle^{-1}$ is the harmonic mean projected separation between galaxy pairs. The mean velocity ($\bar{v}$), velocity dispersion ($\sigma_{\rm v}$), and the virial masses of the clusters, thus estimated, are given in Table 10. The underlying assumption in the relation used is that the galaxies included in each of the clusters are bound and their velocity dispersions are isotropic. The virial masses obtained for the two clusters have large errors (especially for A3530) and therefore do not differ significantly. A better estimation of the virial masses requires more redshift data for both the clusters.

[4] The values of R_{200} (radius within which the mean density of the cluster equals 200 times the critical density) obtained by Vulcani et al. (2011; 1.50 Mpc for A3532 and 1.36 Mpc for A3530) have been used.

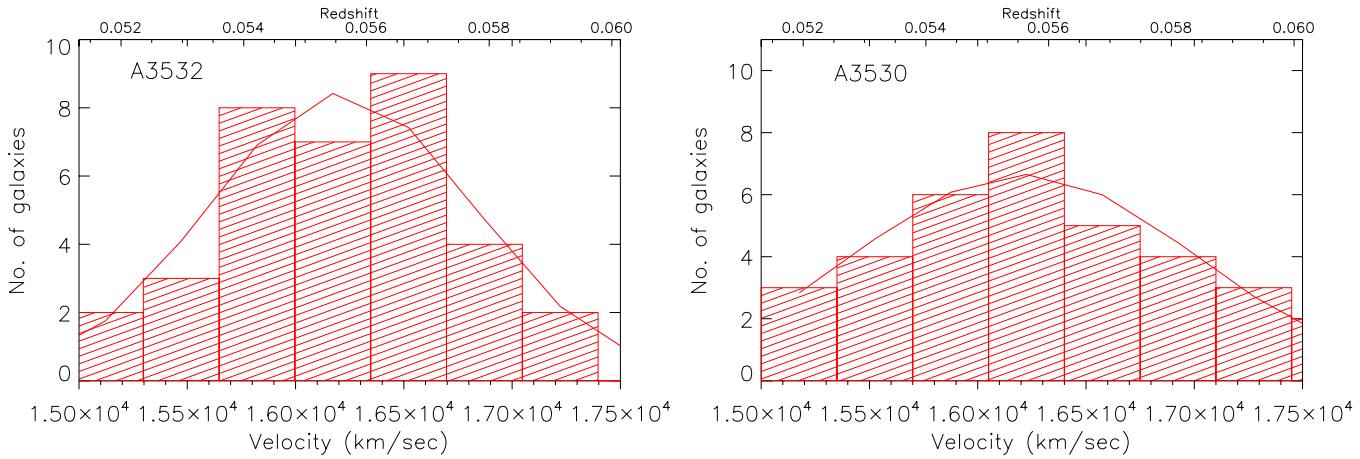

Figure 14. Galaxy velocity histograms for the clusters A3532 (left) and A3530 (right) overlaid with the Gaussian fits. The bin size used for both the clusters is 350 km s^{-1}.

(A color version of this figure is available in the online journal.)

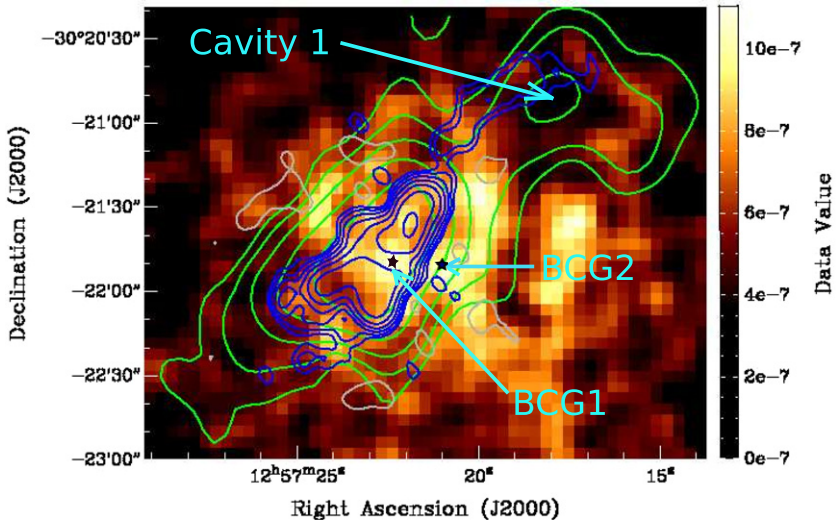

Figure 15. Exposure-corrected and point-source-removed *Chandra* ACIS images of the central part of A3532 in the 0.3–7.0 keV band, smoothed using a Gaussian kernel of width 4″, and overlaid with the GMRT 50 cm contours (blue; levels the same as in Figure 4(c)), and the TGSS 2 m radio contours (green; levels the same as in Figure 4(e)). Positions of the two brightest galaxies (BCG 1 and BCG 2; marked with black stars) and the candidate cavity (cavity 1) have been shown.

(A color version of this figure is available in the online journal.)

Table 10
The Values of Virial Mass and the Parameters Used (Derived in Section 4.8) for A3532 and A3530

Cluster	No. of Galaxies	$\bar{v}$ (km s^{-1})	σ_v (km s^{-1})	M_{virial} (10^{14} $M_\odot$)
A3532	40	16211 ± 157	615 ± 159	3.4 ± 1.8
A3530	35	16213 ± 246	794 ± 286	5.5 ± 4.0

Note. Errors are quoted at 90% confidence level based on χ^2_{min}+2.71.

4.9. X-Ray–Radio Interaction

Figure 15 shows a moderately smoothed (Gaussian kernel width ∼4″) *Chandra* image of the central part of the cluster, overlaid with the GMRT 50 cm (blue) and TGSS 2 m (green) contours. The image shows highly anisotropic X-ray emission with four main peaks at the center. The brightest peak coincides with the brighter nucleus of the dumbbell BCG (shown as BCG 1). Another adjacent peak is seen toward its west, coinciding with the position of the second nucleus of the dumbbell BCG (shown as BCG 2). Two more peaks are seen at distances of about 1′ and 40″, northwest from the center of the brightest peak. The image also shows a number of apparent cavities or depressions in the X-ray surface brightness, both on large scales and small scales, and in various parts of the cluster. However, because of the very small exposure time of the *Chandra* observation, the detection significance of these cavities is very low. In the following analysis, we have focused on one "candidate" cavity which is most prominent and visible in the *Chandra* images at all resolutions. In Figure 15, the northwestern radio extension of the WAT in both sets of radio contours seems to coincide with a large-scale candidate cavity ("cavity 1", hereafter) and in the TGSS 2 m contours (green), it seems to fill the cavity completely. To estimate the significance of "cavity 1", we used the X-ray surface brightness profile, made by using annular sectors along the direction of the cavity (see Figure 16). "Cavity 1" shows up as a significant dip (∼4σ average; ∼5σ at the minimum) in the X-ray surface brightness profile. It seems possible that the "cavity 1" and the radio emission from the WAT are related to each other. Assuming "cavity 1" is indeed real, we have investigated the energy requirements of the cavity, below.

Table 11
Energetics of the Candidate "Cavity 1" (See Section 4.9)

R_1 (kpc)	R_2 (kpc)	R (kpc)	P (10^{-11} erg cm^{-3})	V (10^{69} cm^3)	E_{cav} (10^{59} erg)	t_{cav} (10^7 yr)	P_{cav} (10^{43} erg s^{-1})	L_{radio} (10^{43} erg s^{-1})
23.9	21.3	22.6	2.2	1.2	1.2	7.5	4.6	$0.06^{+0.03}_{-0.02}$

Notes. R_1, R_2, and R represent the semi-major axis, the semi-minor axis, and the average radius ($=\sqrt{R_1 R_2}$) of the approximate ellipses describing the cavities, respectively. P is the pressure of the hot gas surrounding the cavities, V is the volume of the (prolate) ellipsoidal cavities, E_{cav} is the total energy required to create the cavities, t_{cav} is the cavity age, P_{cav} is the jet power required, and L_{radio} is the 10 MHz–10 GHz integrated radio power of the WAT source. Details are given in Section 4.9.1.

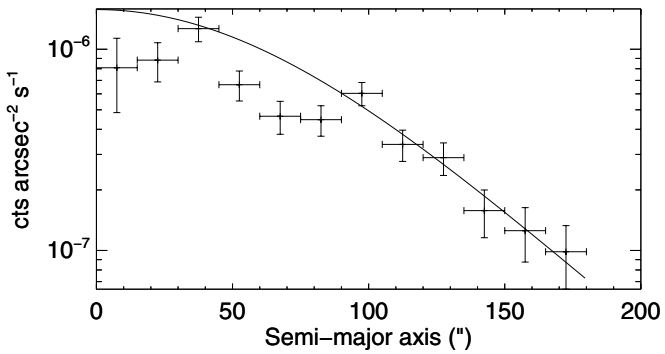

Figure 16. Profile of the X-ray surface brightness along "cavity 1" (see Figure 15), made by using 12 annular sectors along the direction of the cavity. A β-model ($S(x) = S_0(1 + (x/R_c)^2)^{-3\beta+0.5}$) has been fitted to the profile, excluding the three data points corresponding to the dip and the initial two points that show the central surface brightness fluctuations. The significance of the dip averaged over the cavity is $\sim 4\sigma$ and at the minimum is $\sim 5\sigma$.

4.9.1. Cavity Energetics

The total energy required to create a cavity (E_{cav}) is the sum of the work done in expanding the cavity ($=\int -P\, dV = PV/(\gamma-1)$) plus the energy in the cavity ($= PV$) (see Dunn & Fabian 2004), where P is the pressure of the hot gas surrounding the cavity, V is the volume of the cavity, and γ is the ratio of the specific heats ($= c_p/c_v$). By using $\gamma = 4/3$ for the relativistic jets, we obtain, $E_{cav} = \gamma PV/(\gamma - 1) = 4PV$ (see Bîrzan et al. 2004; McNamara & Nulsen 2007, 2012; Fabian 2012). The power required by the jet to create the cavity (P_{cav}) is given by the total energy of the cavity divided by the age of the cavity. For our analysis, we have approximated the age of the cavity (t_{cav}) as the sound crossing time, which is the time taken by the sound waves to travel from the center of the AGN to the current location of the cavity (see Hlavacek-Larrondo et al. 2012). The pressure of the hot gas and the density (required for calculating the sound speed) have been estimated by using their approximate average values at the location of the cavities in the thermodynamic maps. To estimate the volumes of the cavities, prolate ellipsoidal shapes were assumed. The semi-major and semi-minor axes (R_1 and R_2) of the ellipse, the average radius R ($=\sqrt{R_1 R_2}$), the pressure of the hot gas surrounding the cavity (P), the volume of the cavity (V), the total energy required for the cavity (E_{cav}), the age of the cavity (t_{cav}), and the power of the jets required (P_{cav}) to create the cavity, calculated for the "cavity 1", are given in Table 11. Here, it should be noted that the errors associated with the shape and volume of the ellipse used to describe the cavity 1 were very large ($\sim$30%–80%) because of the very crude approximation and also because of the projection effects.

We have also calculated the radio power (luminosity) of the WAT source (L_{radio}) by integrating $L_\nu = 4\pi D_L^2 S_\nu$, from 10 MHz to 10 GHz. D_L is the luminosity distance to the source, $S_\nu (\propto \nu^\alpha)$ is the flux density at frequency ν, and α is the radio spectral index of the WAT. The radio power so obtained is given in Table 11. L_{radio} is found to be lower than P_{cav}, by about a factor of 80. Note that P_{cav} might have errors as large as 70% due to the very crude approximation of the shape of the cavity and additional errors in the pressure of the hot gas and the age of the cavity. Figure 17 shows the relationship between the jet power required to create the cavity and the radio power (integrated for the 10 MHz−10 GHz band) reproduced from O'Sullivan et al. (2011; OS11, hereafter). The sample shown in the figure is based on cavities found in the nine groups of galaxies studied by OS11 and 24 groups of galaxies studied by Bîrzan et al. (2008; B08, hereafter). The point corresponding to the "cavity 1" (shown with a blue color) is found to be well within the scatter in Figure 17. This result further supports that "cavity 1" and the radio emission from the WAT might be related to each other. The temperature in the box region at the location of "cavity 1" in Figure 11(a) is found to be marginally higher than that in the immediately surrounding boxes. There is a possibility that the

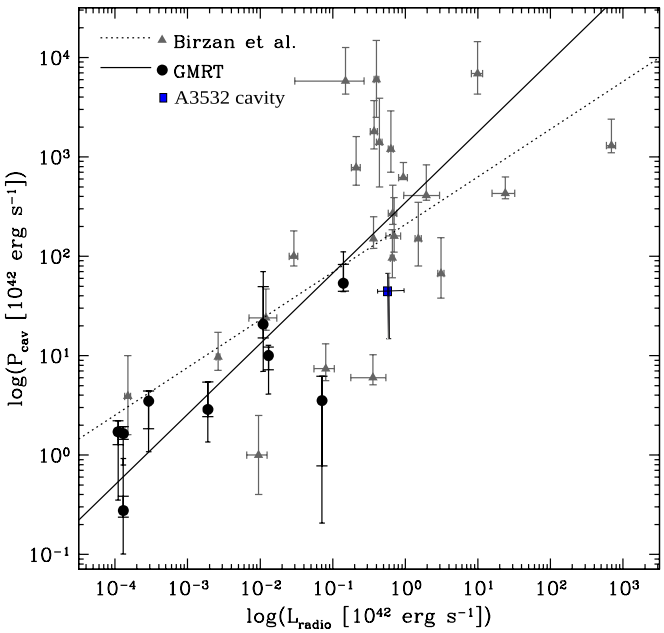

Figure 17. Jet power required to create the cavity P_{cav} vs. the 10 MHz–10 GHz integrated radio power L_{radio}, reproduced from OS11 (see Section 4.9.1). The 24 gray triangles and 9 black circles are corresponding to the cavities studied by B08 and OS11, respectively. The solid line indicates the bivariate correlated errors and intrinsic scatter (BCES) fit obtained by OS11 for all the data points (triangles plus circles). The dotted line indicates the relation found by B08 for only the 24 cavities studied by them. The blue box is the point corresponding to the "cavity 1".

(A color version of this figure is available in the online journal.)

"cavity 1" is formed by the energy deposited into the ICM by the radio jets of the WAT source in A3532 from a past central AGN outburst. In that case, P_{cav} can provide an estimate for the energy released during that AGN outburst. From the results obtained by Bîrzan et al. (2004) and Rafferty et al. (2006), we find that the typical observed deficit in the cooling luminosity of clusters with X-ray cavities is between 10–1000 $\times$ 10^{42} erg s^{-1} and for a cluster with A3532-like bolometric X-ray luminosity, it is $\sim$400 $\times$ 10^{42} erg s^{-1}. P_{cav} for "cavity 1" is about one-tenth of this value (see Table 11). One can, therefore, speculate that only the combined effect of a few such past outbursts could have led to the disruption of the cool core in A3532 (see Bîrzan et al. 2004; Dunn et al. 2005, 2010; Rafferty et al. 2006). However, due to the short exposure of the *Chandra* observation, it is not possible to reliably estimate and compare the deficit in the cooling luminosity of A3532 and the total energy requirements of all the X-ray cavities in it.

5. DISCUSSION AND CONCLUSIONS

The combined image of the diffuse X-ray emission of the cluster pair A3532–A3530 shows excess X-ray emission in an OR between the clusters (Figure 1). In the thermodynamic maps described in Section 4.5, this OR is found to have a significantly lower temperature and abundance than the clusters themselves, thereby nullifying the possibility of cluster scale mergers taking place between them. This observation is in agreement with the findings of Mauduit & Mamon (2007; see Section 1). The results obtained by us can have two possible interpretations. In the first scenario, the clusters are approaching each other for the first time and are tidally interacting in their OR, as a precursor to a possible merger at a later time. The interaction between the two clusters has just started and, therefore, the X-ray gas in the OR is neither very hot nor highly enriched with metals. In the second possible scenario, the individual X-ray halos of the two clusters are well separated from each other and the OR seen between the clusters is merely due to their chance superposition (see Section 1). However, from our analysis of the galaxy velocity information available for the clusters (see Section 4.8), both A3532 and A3530 seem to be at the same redshift, and therefore, we believe that the probability of the OR being a result of a chance superposition is very low.

A3530 shows almost constant or smoothly varying thermodynamic maps and profiles. Therefore, no significant merger activity within A3530 could be detected. However, there are many indications of ongoing galaxy scale mergers in the inner regions of the cluster A3532. These are described in the following. First, the average temperature of A3532 is significantly higher than that of A3530. Second, the thermodynamic maps show high temperature regions in various parts of the cluster. Third, it is seen to host a dumbbell system of BCGs at its center, and the brighter nucleus of the dumbbell contains a WAT radio source, which is mostly seen in merging clusters of galaxies. However, gravitational interaction between the galaxies of the dumbbell may also be responsible for the presence of the WAT. The overall geometry of the WAT, which has very closely aligned tails, may be attributed to the projection effects due to an apparently small angle between the plane of the WAT and our line of sight. At low frequencies, the radio emission shows an extension toward the northwest, which is either a part of the WAT radio emission or a separate source. The extension seems to have a steep spectrum and a rough estimate of the power-law spectral index is close to -2.

The bolometric X-ray luminosities of the two clusters are found to be close to those of the rich clusters but with slightly higher average temperatures. While a high temperature in A3532 is possibly due to ongoing galaxy scale mergers in its inner regions, high temperature in A3530 is not clear. However, an interaction between the pair of galaxies located at the center of A3530 may have resulted in increasing the temperature. A deeper exposure with the *Chandra* will be required to test this scenario.

The gas mass estimates of the clusters (Section 4.7) show A3532 to be marginally more massive than A3530, while their virial mass estimates (Section 4.8) have large errors and do not show any significant difference. On comparing with the M_{500} estimates of the two clusters obtained by Ettori et al. (1997; see Section 1), the virial mass obtained by us for A3530 is found to be consistent while that for A3532 is smaller. This discrepancy is probably because the method used by Ettori et al. and the underlying assumptions were different from our analysis and also because a small number of galaxies was used for the virial mass estimation, which might have led to large errors in fitting the galaxy velocity distribution.

A3532 and A3530 have been classified as non-cooling flow clusters in the literature (see Section 1). The cooling time estimates of both clusters (see Section 4.6) are also found to be close to the Hubble time, as is observed for the NCC clusters. However, A3530 shows some other properties which are similar to the cool core clusters. A significantly low value of the deprojected temperature is found at its center, where the temperature drops to about $\sim$70% of the average value obtained for the cluster (see Section 4.4.2). The elemental abundance in A3530 is found to peak at the center (see Section 4.4.1), with a gradual decrease outward. Negative metal abundance gradients are typical of cool core clusters (Johnson et al. 2011; De Grandi & Molendi 2001; Irwin & Bregman 2001; Finoguenov et al. 2000). The projected global and central values of elemental abundance for A3530 obtained by us ($0.28^{+0.05}_{-0.04}$ and $0.48^{+0.16}_{-0.14}$ solar, respectively) are consistent with those of the cool core clusters (0.37 ± 0.4 and 0.42 ± 0.06 solar, respectively; Irwin & Bregman 2001). In addition, A3530 shows smooth, isotropic, and centrally peaked profiles of X-ray surface brightness and the thermodynamic quantities (see Sections 4.1, 4.4.1, 4.4.2, and 4.5), which are usually found in the relaxed cool core clusters. Based on all these observations, the possibility of a weak cool core in A3530 cannot be ignored. To confirm the weak cool core, deeper high-resolution X-ray observations of the central region of A3530 will be required. A3532, unlike A3530, shows many properties similar to the NCC clusters, e.g., the presence of high temperature regions at the center as well as in the other parts of the cluster, anisotropic variations in the X-ray surface brightness and thermodynamic maps, and no definite trend in the abundance profile of the cluster. A3532, therefore, seems to be an NCC cluster where cooling flows may have been disrupted by past activity in the central AGN (see Fabian 2002; McNamara & Nulsen 2007; Mittal et al. 2009; Baldi et al. 2009; Ehlert et al. 2011; and the discussion given in Section 4.9.1 of this paper).

In agreement with the findings of Pimbblet (2008), neither cluster shows any signs of subclustering in either optical or large-scale ($\sim$5′) X-ray emission, which is believed to be a prerequisite for an ongoing merger. However, in the high-resolution *Chandra* images of A3532 (Figures 3 and 15), we do see the presence of small-scale (20″) substructures in its central region. The *Chandra* images show a distorted X-ray

structure and multiple peaks in the core of the cluster, which are probably a result of the stripping of the hot gas of the less bright dumbbell galaxy either due to tidal interaction or due to the ram pressure stripping resulting from its motion through the dense ICM, similar to what is observed in the dumbbell galaxies NGC 4782 and NGC 4783 (Machacek et al. 2007). The X-ray image also shows many candidate cavities in the central part of A3532 both at large scales ($\sim 30''$) and small scales ($\sim 10''$). Of these, a large-scale cavity ("cavity 1") seems to coincide with the northwestern extension of the WAT source, seen in the low-frequency radio images (Figure 5). The average significance of "cavity 1" is found to be $\sim 4\sigma$. Further, in Section 4.9.1, the radio luminosity of the WAT source seems to be related to the power of the jets required to create the cavity. If "cavity 1" is indeed real then, based on these results, it is possible that it is created by a buoyantly rising radio bubble emanating from the WAT source. The other less-significant, non-radio cavities may be "ghost" cavities, which are relics of past radio outbursts from the central AGN in the cluster where the radio emission has probably faded due to a stopped supply of relativistic particles from the nucleus (Clarke et al. 2007; McNamara et al. 2001). Deeper and high-resolution, X-ray and low-frequency radio observation of A3532 are required for significant detection of all the cavities, to accurately study the morphological and spectral properties of the weak radio emission features in the cluster, and to ascertain a connection between the X-ray and radio emission from the cluster.

The X-ray data used in this research have been obtained from the High Energy Astrophysics Science Archive Research Center (HEASARC), provided by NASA's Goddard Space Flight Center. We have used observations obtained with *XMM-Newton*, an ESA science mission with instruments and contributions directly funded by ESA member states and the USA (NASA), and the *Chandra X-Ray Observatory*, managed by NASA's Marshall Center. We thank the *Chandra* and *XMM* helpdesk for their assistance on X-ray data analysis. Data were also obtained from the Australia Telescope Compact Array which is a part of the Australia Telescope National Facility, funded by the Commonwealth of Australia for operation as a National Facility managed by CSIRO. We have also made use of the survey data from the TGSS (http://tgss.ncra.tifr.res.in) with the GMRT, and from the VLSS and NVSS with the VLA. VLA is maintained by the NRAO, which is a facility of the National Science Foundation operated under cooperative agreement by Associated Universities, Inc. Finally, we thank the anonymous referee for his valuable comments and suggestions that have helped us improve many of our results.

REFERENCES

Abell, G. O., Corwin, H. G., Jr., & Olowin, R. P. 1989, ApJS, 70, 1
Anders, E., & Ebihara, M. 1982, GeCoA, 46, 2363
Baldi, A., Forman, W., Jones, C., et al. 2009, ApJ, 694, 479
Bardelli, S., Pisani, A., Ramella, M., Zucca, E., & Zamorani, G. 1998a, MNRAS, 300, 589
Bardelli, S., Zucca, E., & Baldi, A. 2001, MNRAS, 320, 387
Bardelli, S., Zucca, E., Malizia, A., et al. 1996, A&A, 305, 435
Bardelli, S., Zucca, E., Vettolani, G., et al. 1994, MNRAS, 267, 665
Bardelli, S., Zucca, E., Zamorani, G., Moscardini, L., & Scaramella, R. 2000, MNRAS, 312, 540
Bardelli, S., Zucca, E., Zamorani, G., Vettolani, G., & Scaramella, R. 1998b, MNRAS, 296, 599
Beers, T. C., Geller, M. J., & Huchra, J. P. 1982, ApJ, 257, 23
Bîrzan, L., McNamara, B. R., Nulsen, P. E. J., Carilli, C. L., & Wise, M. W. 2008, ApJ, 686, 859
Bîrzan, L., Rafferty, D. A., McNamara, B. R., Wise, M. W., & Nulsen, P. E. J. 2004, ApJ, 607, 800
Burns, J. O. 1981, MNRAS, 195, 523
Burns, J. O., Rhee, G., Owen, F. N., & Pinkney, J. 1994, ApJ, 423, 94
Carter, J. A., & Read, A. M. 2007, A&A, 464, 1155
Cava, A., Bettoni, D., Poggianti, B. M., et al. 2009, A&A, 495, 707
Chen, Y., Reiprich, T. H., Böhringer, H., Ikebe, Y., & Zhang, Y.-Y. 2007, A&A, 466, 805
Clarke, T., Blanton, E., Sarazin, C. L., et al. 2007, in ESO Astrophysics Symp., Heating versus Cooling in Galaxies and Clusters of Galaxies ed. H. Böhringer, P. Schuecker, G. W. Pratt, & A. Finoguenov (Berlin: Springer), 124
Cohen, A. S., Lane, W. M., Cotton, W. D., et al. 2007, AJ, 134, 1245
Condon, J. J., Cotton, W. D., Greisen, E. W., et al. 1998, AJ, 115, 1693
Cristiani, S., D'Odorico, S., de Souza, R., Lund, G., & Quintana, H. 1987, A&A, 179, 108
de Filippis, E., Schindler, S., & Erben, T. 2005, A&A, 444, 387
De Grandi, S., & Molendi, S. 2001, ApJ, 551, 153
Donnelly, R. H., Forman, W., Jones, C., et al. 2001, ApJ, 562, 254
Douglass, E. M., Blanton, E. L., Clarke, T. E., Sarazin, C. L., & Wise, M. 2008, ApJ, 673, 763
Dressler, A., & Shectman, S. A. 1988, AJ, 95, 985
Dunn, R. J. H., Allen, S. W., Taylor, G. B., et al. 2010, MNRAS, 404, 180
Dunn, R. J. H., & Fabian, A. C. 2004, MNRAS, 355, 862
Dunn, R. J. H., Fabian, A. C., & Taylor, G. B. 2005, MNRAS, 364, 1343
Ehlert, S., Allen, S. W., von der Linden, A., et al. 2011, MNRAS, 411, 1641
Eilek, J. A., Burns, J. O., O'Dea, C. P., & Owen, F. N. 1984, ApJ, 278, 37
Ettori, S., Bardelli, S., De Grandi, S., et al. 2000, MNRAS, 318, 239
Ettori, S., Fabian, A. C., & White, D. A. 1997, MNRAS, 289, 787
Fabian, A. C. 2002, in Proc. MPA/ESO/MPE/USM Joint Astronomy Conf., Lighthouses of the Universe: The Most Luminous Celestial Objects and Their Use for Cosmology, ed. M. Gilfanov, R. Sunyaev, & E. Churazov (Berlin: Springer), 24
Fabian, A. C. 2012, ARA&A, 50, 455
Finoguenov, A., David, L. P., & Ponman, T. J. 2000, ApJ, 544, 188
Gitti, M., O'sullivan, E., Giacintucci, S., et al. 2010, ApJ, 714, 758
Gregorini, L., de Ruiter, H. R., Parma, P., et al. 1994, A&AS, 106, 1
Gu, L.-Y., Wang, Y., Gu, J.-H., et al. 2010, RAA, 10, 1005
Henry, J. P., Finoguenov, A., & Briel, U. G. 2004, ApJ, 615, 181
Hlavacek-Larrondo, J., Fabian, A. C., Edge, A. C., et al. 2012, MNRAS, 421, 1360
Ikebe, Y., Reiprich, T. H., Böhringer, H., Tanaka, Y., & Kitayama, T. 2002, A&A, 383, 773
Irwin, J. A., & Bregman, J. N. 2001, ApJ, 546, 150
Johnson, R., Finoguenov, A., Ponman, T. J., Rasmussen, J., & Sanderson, A. J. R. 2011, MNRAS, 413, 2467
Jones, T. W., & Owen, F. N. 1979, ApJ, 234, 818
Kalberla, P. M. W., Burton, W. B., Hartmann, D., et al. 2005, A&A, 440, 775
Klamer, I., Subrahmanyan, R., & Hunstead, R. W. 2004, MNRAS, 351, 101
Lakhchaura, K., Singh, K. P., Saikia, D. J., & Hunstead, R. W. 2011, ApJ, 743, 78
Large, M. I., Mills, B. Y., Little, A. G., Crawford, D. F., & Sutton, J. M. 1981, MNRAS, 194, 693
Machacek, M. E., Kraft, R. P., Jones, C., Forman, W. R., & Hardcastle, M. J. 2007, ApJ, 664, 804
Mahdavi, A., & Geller, M. J. 2001, ApJL, 554, L129
Mao, M. Y., Johnston-Hollitt, M., Stevens, J. B., & Wotherspoon, S. J. 2009, MNRAS, 392, 1070
Mauch, T., Murphy, T., Buttery, H. J., et al. 2003, MNRAS, 342, 1117
Mauduit, J.-C., & Mamon, G. A. 2007, A&A, 475, 169
McCarthy, I. G., West, M. J., & Welch, G. A. 2002, ApJ, 567, 762
McNamara, B. R., & Nulsen, P. E. J. 2007, ARA&A, 45, 117
McNamara, B. R., & Nulsen, P. E. J. 2012, NJPh, 14, 055023
McNamara, B. R., Wise, M. W., Nulsen, P. E. J., et al. 2001, ApJL, 562, L149
Mittal, R., Hudson, D. S., Reiprich, T. H., & Clarke, T. 2009, A&A, 501, 835
Morrison, R., & McCammon, D. 1983, ApJ, 270, 119
O'Donoghue, A. A., Owen, F. N., & Eilek, J. A. 1990, ApJS, 72, 75
O'Sullivan, E., Giacintucci, S., David, L. P., et al. 2011, ApJ, 735, 11
Owen, F. N., & Rudnick, L. 1976, ApJL, 205, L1
Parma, P., de Ruiter, H. R., & Cameron, R. A. 1991, AJ, 102, 1960
Pimbblet, K. A. 2008, PASA, 25, 176
Pisani, A. 1993, MNRAS, 265, 706
Pisani, A. 1996, MNRAS, 278, 697
Planelles, S., & Quilis, V. 2009, MNRAS, 399, 410

Rafferty, D. A., McNamara, B. R., Nulsen, P. E. J., & Wise, M. W. 2006, ApJ, 652, 216
Raychaudhury, S., Fabian, A. C., Edge, A. C., Jones, C., & Forman, W. 1991, MNRAS, 248, 101
Reiprich, T. H., & Böhringer, H. 2002, ApJ, 567, 716
Roettiger, K., Burns, J. O., & Loken, C. 1996, ApJ, 473, 651
Sarazin, C. L. 1988, X-Ray Emission from Clusters of Galaxies (Cambridge Astrophysics Series; Cambridge: Cambridge Univ. Press)
Sarazin, C. L. 2002, in Merging Processes in Galaxy Clusters, ed. L. Feretti, I. M. Gioia, & G. Giovannini (Astrophysics and Space Science Library, Vol. 272; Dordrecht: Kluwer), 1
Sault, R. J., Teuben, P. J., & Wright, M. C. H. 1995, in ASP Conf. Ser. 77, Astronomical Data Analysis Software and Systems IV, ed. R. A. Shaw, H. E. Payne, & J. J. E. Hayes (San Francisco, CA: ASP), 433
Schindler, S. 1996, MNRAS, 280, 309
Shapley, H. 1933, PNAS, 19, 591
Smith, R. K., Brickhouse, N. S., Liedahl, D. A., & Raymond, J. C. 2001, ApJL, 556, L91
Snowden, S. L., & Kuntz, K. D. 2011, BAAS, 43, 34457
Snowden, S. L., Mushotzky, R. F., Kuntz, K. D., & Davis, D. S. 2008, A&A, 478, 615
Strüder, L., Briel, U., Dennerl, K., et al. 2001, A&A, 365, L18
Turner, M. J. L., Abbey, A., Arnaud, M., et al. 2001, A&A, 365, L27
Venturi, T., Bardelli, S., Morganti, R., & Hunstead, R. W. 1997, MNRAS, 285, 898
Venturi, T., Bardelli, S., Morganti, R., & Hunstead, R. W. 1998, MNRAS, 298, 1113
Venturi, T., Bardelli, S., Morganti, R., & Hunstead, R. W. 2000, MNRAS, 314, 594
Venturi, T., Bardelli, S., Zambelli, G., Morganti, R., & Hunstead, R. W. 2001, MNRAS, 324, 1131
Vettolani, G., Chincarini, G., Scaramella, R., & Zamorani, G. 1990, AJ, 99, 1709
Vogeley, M. S., Park, C., Geller, M. J., Huchra, J. P., & Gott, J. R., III 1994, ApJ, 420, 525
Vulcani, B., Poggianti, B. M., Dressler, A., et al. 2011, MNRAS, 413, 921
Wirth, A., Smarr, L., & Gallagher, J. S. 1982, AJ, 87, 602
Xue, Y.-J., & Wu, X.-P. 2000, ApJ, 538, 65